ENTROPY PRODUCTION IN VISCOELASTIC FLUID FLOWS IN A ROTATING FRAME WITH HEAT DISSIPATION USING OPTIMAL HOMOTOPY ANALYSIS METHOD (OHAM)

By

Sana Fakhar

(Registration No: 00000402965)

A thesis submitted to the National University of Sciences and Technology, Islamabad,

in partial fulfillment of the requirements for the degree of

Master of Science in Mathematics

Supervisor: **Prof. Meraj Mustafa Hashmi**

School of Natural Sciences, National University of Sciences & Technology (NUST), Islamabad, Pakistan

(2024)

THESIS ACCEPTANCE CERTIFICATE

Certified that final copy of MS thesis written by **Sana Fakhar** (Registration No **00000402965)**, of **School of Natural Sciences** has been vetted by undersigned, found complete in all respects as per NUST statutes/regulations, is free of plagiarism, errors, and mistakes and is accepted as partial fulfillment for award of MS/M.Phil degree. It is further certified that necessary amendments as pointed out by GEC members and external examiner of the scholar have also been incorporated in the said thesis.
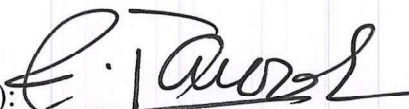
Signature: _____

Name of Supervisor: Prof. Meraj Mustafa Hashmi

Date: _____5/9/2024_____

Signature (HoD): _____

Date: ___5/9/2024___

Signature (Dean/Principal): _____

Date: ___05-09-2024___

National University of Sciences & Technology

MS THESIS WORK

We hereby recommend that the dissertation prepared under our supervision by: Sana Fakhar, Regn No. 00000402965 Titled Entropy Production in Viscoelastic Fluid Flows in a Rotating Frame with Heat Dissipation Using Optimal Homotopy Analysis Method (OHAM) be Accepted in partial fulfillment of the requirements for the award of MS degree.

Examination Committee Members

1. Name: PROF. MUJEEB UR REHMAN   Signature:

2. Name: DR. RIZWAN UL HAQ   Signature:

Supervisor's Name PROF. MERAJ MUSTAFA HASHMI   Signature:

_____   5/9/2024
Head of Department   Date

COUNTERSINGED

Date: 05-09-2024   Dean/Principal

DEDICATION

This thesis is dedicated to my beloved parents. I would also like to extend my heartfelt appreciation to my wonderful supervisor for his invaluable guidance and endless efforts.

TABLE OF CONTENTS

I

LIST OF TABLES

LIST OF FIGURES

ABSTRACT

The exploration of rotational dynamics within fluid motion holds profound importance across diverse fields such as industrial chemical processes, advancements in food processing technologies, the optimization of turbomachinery, efficient cooling techniques for computer storage drives and various other applications. This study assesses entropy creation in MHD viscoelastic flow using the intriguing Walters-B and Jeffery model over a linearly deforming plate within a rotating frame of reference. The inclusion of Coriolis and centrifugal forces due to the rotating frame introduces additional terms in the momentum balance equation. Furthermore, the energy equation, which includes terms for viscous dissipation and Joule heating, is examined. The representative non-linear problem is analyzed through optimal homotopy analysis method (OHAM) available within the "MATHEMATICA" package "BVPh 2.0". This routine is implemented to retrieve the optimal auxiliary parameters and corresponding averaged squared residuals for varying homotopy approximations. The drag on the plate and the surface cooling rate are assessed under the rotating fluid assumption, with varying material parameter of the Walters-B and Jeffery model. Additionally, the impact of heat dissipation on the overall heat transport phenomenon is thoroughly examined.

Keywords: Coriolis force; Walters-B model; Jeffery model; Optimal homotopy method (OHAM); Squared residual

CHAPTER 1:

Introduction

This chapter comprises key concepts, definitions and principles related to the problems narrated in this thesis. The equations governing the dynamics of Walters-B and Jeffrey fluids within a rotating frame of reference are outlined here. Furthermore, an extensive review of the literature related to the flow situations addressed in the following chapters has been carried out. Additionally, a brief discussion is provided on the optimal homotopy scheme and its implementation using Mathematica's BVPH 2.0 routine.

 1.1 Fundamental definitions

1.1.1. Compressible and incompressible flows

In compressible flows, there are substantial variations in fluid density with respect to time, temperature, and pressure. The flows in which fluid density remains unchanged by variations in time and spatial coordinates are classified as incompressible flows. A dimensionless measure known as Mach number distinguishes between compressible and incompressible flows. A flow is categorized as compressible if its Mach number is greater than 0.3 and incompressible if it is less than 0.3.

1.1.2. Steady and unsteady flows

A steady flow is the one in which all flow conditions including velocity, pressure, and density are consistent with time. In unsteady flow, any fluid property may vary over time. In mathematical terms,

$$\frac{\partial \alpha}{\partial t} = 0,$$
(1.1)

here, α represents any fluid's physical property.

1.1.3. Laminar and turbulent flows

Smooth fluid motion in parallel, ordered layers with no interruption between them is regarded as laminar flow. In this kind of flow, the fluid tends to travel without mixing and

streamlines do not overlap one another. On contrary, turbulent flows occurs when at relatively higher velocities the adjacent layers mix and intersect, creating an erratic and disordered flow behavior. Flows are likely to be laminar at low Reynolds number ($Re < 2300$) whereas turbulent flows have comparatively higher Reynolds number ($Re > 4000$).

1.1.4. Newtonian fluids

In Newtonian fluids, the stress-strain curve shows a linear relationship and does not contain origin in general. These fluids satisfy the following relationship:

$$\tau = \mu \mathbf{A}_1, \tag{1.2}$$

in which μ shows the dynamic viscosity, $\mathbf{A}_1 = (\nabla V) + (\nabla V)^t$ represents the first Rivlin-Ericksen tensor and τ denotes the stress tensor. Well-known examples of Newtonian fluids are water, air, and synthetic oils.

1.1.5. Non-Newtonian fluids

Contrary to Newtonian fluids, non-Newtonian fluids do not obey Newton's law of viscosity. In these fluids, viscosity alters with the variations in share rate. Numerous non-Newtonian fluids follow a pattern that can be characterized by a power law equation in unidirectional flow:

$$\tau_{yx} = \xi \frac{du}{dy^*}, \tag{1.3}$$

here $\xi = \gamma(du/dy)^{m-1}$ represents fluid apparent viscosity where ξ indicates the consistency index and m shows the flow behavioral index. Eq. (1.3) corresponds to the Newtonian fluid situation for $m = 1$.

Shear-thinning fluids: For $m < 1$, fluid is characterized as shear-thinning or pseudoplastic as it exhibits an inverse relationship between stress and shear rate. Ketchup, paints, blood, shampoo and certain gels are some of examples.

Shear-thickening fluids: When $m > 1$, the fluid's viscosity increases at a higher shear rate and it is classified as shear-thickening or dilatant fluid. Interesting dilatant-type fluids are oobleck, whipped cream and quicksand.

1.1.6. Viscoelastic fluids

Viscoelastic fluids are classified as special type of non-Newtonian fluid that possesses both viscous and elastic properties while experiencing deformation. These fluids therefore have the characteristics of both solid and liquid illustrating the traits including viscosity, elasticity, and deformation ability. Paints, slurries, polymeric liquids and some biological fluids including blood are well-known viscoelastic fluids. A viscoelastic fluid behaves like a Newtonian fluid and exhibits solid-like behavior when subjected to high stress and returns to its original position upon removal of stress.

1.2. Boundary layer flows

Boundary layer flow is described as the flow of fluid in thin layer adjacent to surface, where the viscous effects are substantial due to existence of frictional forces. The fluid's velocity is zero due to non-slip condition near stationary surface within boundary layer and it increases continuously from zero to free-stream velocity. The thermal boundary layer is a region in fluid flow where temperature gradients are developed due to heat transfer between the fluid and the surface. Basically, in the thermal boundary layer the conduction and convection influences the temperature near the surface.
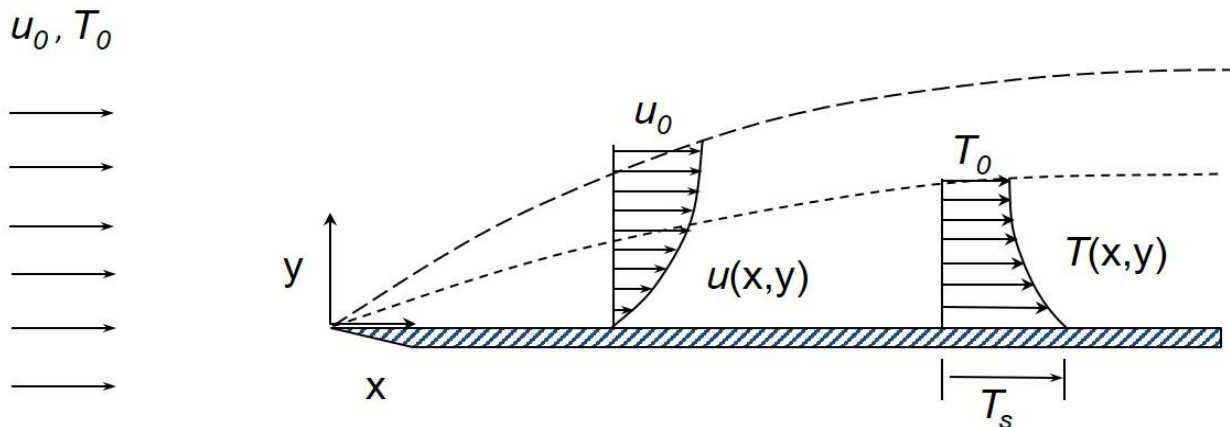
Fig 1.1: Boundary layer formations over a flat surface (Source: Internet).

1.2.1. Boundary layer thickness

Boundary layer thickness is described as the distance from the surface at which the fluid's velocity is zero to the point where the velocity attains free-stream velocity where the fluid's velocity is

approximately equal to ambient velocity such as $u = 0.99U_\infty$, here u is the flow velocity and U_∞ is the free stream velocity. Boundary layer thicknesses that are most frequent are:

- Momentum thickness
- Thermal thickness

1.3. Boundary layer flow over stretching surface in a rotating fluid

We considered the problem in which incompressible and steady fluid flows over a stretchable surface that extends horizontally in the x-direction with velocity $u = ax$, where $a > 0$ is constant. Let u, v be the corresponding representative velocities along the deforming surface and w normal to the surface. Since we have assumed the flow in a rotating frame of reference, Coriolis and centrifugal forces will emerge as a result.

Coriolis force: $F_c = 2\mathbf{\Omega} \times \mathbf{v} = [-2\Omega v, 2\Omega u, 0]$

Centrifugal force: $F_b = \mathbf{\Omega} \times (\mathbf{\Omega} \times \boldsymbol{r}) = [-\Omega^2 x, -\Omega^2 y, 0]$

Surface and ambient temperatures are expressed as T_s and T_∞ respectively. This problem is governed by the following equation:

$$u_x + v_y + w_z = 0, \tag{1.4}$$

$$uu_x + vu_y + wu_z - 2\Omega v = vu_{zz} - \frac{\sigma B_0^2 u}{\rho}, \tag{1.5}$$

$$uv_x + vv_y + wv_z + 2\Omega u = vv_{zz} - \frac{\sigma B_0 v}{\rho}, \tag{1.6}$$

$$uT_x + vT_y + wT_z = \frac{\kappa}{\rho C_p} T_{zz} + \frac{v}{C_p}(u_z^2 + v_z^2) + \frac{\sigma B_0^2}{\rho C_p}(u^2 + v^2). \tag{1.7}$$

Eqs. (1.4)-(1.7) are solved by taking in account the following boundary conditions:

$$u = u_w(x) = ax, \quad v = 0, \quad w = 0, \quad T = T_w(x) \text{ at } z = 0, \tag{1.8}$$

$$u \to 0, \quad u_z \to 0, \quad v \to 0, \quad v_z \to 0, \quad T \to T_\infty \text{ as } z \to \infty. \tag{1.9}$$

A similar solution to the problem is given as follows;

$$u = axf'(\xi), \quad v = axg(\xi), \quad w = -f(\xi)\sqrt{av}, \quad \theta(\xi) = \frac{T - T_\infty}{T_w - T_\infty}, \tag{1.10}$$

where ξ represents the similarity variable. The system of Ordinary differential equations (ODEs) is obtained by substituting transformation in Eqs. (1.4)-(1.9):

$$f''' - f'^2 + ff'' + 2\lambda g - Mf' = 0, \tag{1.11}$$

$$g'' - f'g + fg' - 2\lambda f' - Mg = 0, \tag{1.12}$$

$$\theta'' + Pr(\theta'f - 2\theta f') + PrEc\big(f''^2 + g'^2 + M(f'^2 + g^2)\big) = 0, \tag{1.13}$$

$$f = 0, \quad g = 0, \quad f' = 1, \quad \theta = 1 \quad \text{at} \quad \xi = 0, \tag{1.14}$$

$$f' \to 0, \quad f'' \to 0, \quad g \to 0, \quad g' \to 0, \quad \theta \to 0 \quad \text{as} \quad \xi \to \infty. \tag{1.15}$$

where $Pr = \mu C_p/\kappa$ represents Prandtl number, $Ec = a^2/C_p b$ signifies Eckert number, $M = \sigma B_0^2/\rho a$ is magnetic field parameter, $\lambda = \Omega/a$ is termed as rotation parameter.

1.3.1. Optimal homotopy analysis method (OHAM)

The Homotopy Analysis Method (HAM) was developed by Liao in his 1992 PhD dissertation. This technique is capable of addressing a broad range of nonlinear boundary value problems. Furthermore, it possesses several advantages that set it apart from other analytical methods. For example, unlike the traditional perturbation schemes, the HAM does not depend upon the presence of small/large parameter in the differential equation. The HAM offers significant flexibility in choosing suitable base functions, linear operators and initial estimates. Additionally, it has a distinct method for fine-tuning and managing the convergence of the series solution by choosing specific auxiliary parameters. Here we demonstrate the application of homotopy scheme for the non-linear problem stated through Eqs. (1.11)-(1.13). We begin with selecting the following non-linear operators:

$$\mathcal{L}_f(f) = \frac{d^3 f}{d\xi^3} - \frac{df}{d\xi}, \quad \mathcal{L}_g(g) = \frac{d^2 g}{d\xi^2} - g, \quad \mathcal{L}_\theta(\theta) = \frac{d^2 \theta}{d\xi^2} - \theta, \tag{1.16}$$

The initial approximations for f, g and θ are stated in the following form that satisfies the boundary condition given by Eqs. (1.14) and (1.15):

$$f_0(\xi) = 1 - e^{-\xi}, \quad g_0(\xi) = 0, \quad \theta_0(\xi) = e^{-\xi}, \tag{1.17}$$

The zeroth order deformation equations related to Eqs. (1.11)-(1.13) with boundary condition Eq. (1.14)-(1.15) are presented below where $p \in (0,1)$ is an embedding parameter and $\hbar_f$, $\hbar_g$ and $\hbar_\theta$ are the non-zero auxillary parameters.

$$(1 - p)\mathcal{L}_f\{\hat{f}(\xi; p) - f_0(\xi)\} = p\hbar_f N_f\{\hat{f}(\xi; p), \hat{g}(\xi; p)\}, \tag{1.18}$$

$$(1 - p)\mathcal{L}_g\{\hat{g}(\xi; p) - g_0(\xi)\} = p\hbar_g N_g\{\hat{f}(\xi; p), \hat{g}(\xi; p)\}, \tag{1.19}$$

$$(1 - p)\mathcal{L}_\theta\{\hat{\theta}(\xi; p) - \theta_0(\xi)\} = p\hbar_\theta N_\theta\{\hat{f}(\xi; p), \hat{\theta}(\xi; p)\}, \tag{1.20}$$

$$\hat{f}(\xi; p)|_{\xi=0} = 0, \quad \frac{\partial \hat{f}(\xi; p)}{\partial \xi}\Big|_{\xi=0} = 1, \quad \hat{g}(\xi; p)|_{\xi=0} = 0, \quad \hat{\theta}(\xi; p)|_{\xi=0} = 1, \tag{1.21}$$

$$\frac{\partial \hat{f}(\xi; p)}{\partial \xi}\Big|_{\xi \to \infty} = \frac{\partial^2 \hat{f}(\xi; p)}{\partial \xi^2}\Big|_{\xi \to \infty} = 0, \quad \hat{g}(\xi; p)|_{\xi \to \infty} = \frac{\partial \hat{g}(\xi; p)}{\partial \xi}\Big|_{\xi \to \infty} = 0, \quad \hat{\theta}(\xi; p)|_{\xi \to \infty} = 0, \tag{1.22}$$

where the non-linear operators are mentioned below:

$$N_f = \frac{\partial^3 \hat{f}}{\partial \xi^3} - \left(\frac{\partial \hat{f}}{\partial \xi}\right)^2 + \hat{f}\frac{\partial^2 \hat{f}}{\partial \xi^2} + 2\lambda\hat{g} - M\frac{\partial \hat{f}}{\partial \xi}, \tag{1.23}$$

$$N_g = \frac{\partial^2 \hat{g}}{\partial \xi^2} - \hat{g}\frac{\partial \hat{f}}{\partial \xi} + \hat{f}\frac{\partial \hat{g}}{\partial \xi} - 2\lambda\frac{\partial \hat{f}}{\partial \xi} - M\hat{g}, \tag{1.24}$$

$$N_\theta = \frac{\partial^2 \hat{\theta}}{\partial \xi^2} + Pr\left(\hat{f}\frac{\partial \hat{\theta}}{\partial \xi} - 2\hat{\theta}\frac{\partial \hat{f}}{\partial \xi}\right) + PrEc\left\{\left(\frac{\partial^2 \hat{f}}{\partial^2 \xi}\right)^2 + \left(\frac{\partial \hat{g}}{\partial \xi}\right)^2 + M\left(\left(\frac{\partial \hat{f}}{\partial \xi}\right)^2 + \hat{g}^2\right)\right\}. \tag{1.25}$$

It's important to mention that Eqs. (1.18)-(1.20) represent the initial estimates f_0, g_0 and θ_0 at $p = 0$, with the final solutions being obtained when $p = 1$. Let us expand the functions f, g and θ using the Taylor series about $p = 0$:

$$\hat{f}(\xi; p) = f_0(\xi) + \sum_{k=1}^{\infty} f_k(\xi)p^k, \tag{1.26}$$

$$\hat{g}(\xi; p) = g_0(\xi) + \sum_{k=1}^{\infty} g_k(\xi)p^k, \tag{1.27}$$

$$\hat{\theta}(\xi; p) = \theta_0(\xi) + \sum_{k=1}^{\infty} \theta_k(\xi)p^k, \tag{1.28}$$

where

$$f_k(\xi) = \frac{1}{k!}\frac{\partial^k \hat{f}(\xi;p)}{\partial p^k}\bigg|_{p=0}, \quad g_k(\xi) = \frac{1}{k!}\frac{\partial^k \hat{g}(\xi;p)}{\partial p^k}\bigg|_{p=0}, \quad \theta_k(\xi) = \frac{1}{k!}\frac{\partial^k \hat{\theta}(\xi;p)}{\partial p^k}\bigg|_{p=0}. \quad (1.29)$$

where $f_k(\xi)$, $g_k(\xi)$ and $\theta_k(\xi)$ are calculated through the deformation equations, which are obtained by differentiating the zeroth-order deformation equations k-times and then setting $p = 0$:

$$\mathcal{L}_f\{f_k(\xi) - \mathcal{X}_k f_{k-1}(\xi)\} = \hbar_f \mathcal{R}_k^f(\xi), \quad (1.30)$$

$$\mathcal{L}_g\{g_k(\xi) - \mathcal{X}_k g_{k-1}(\xi)\} = \hbar_g \mathcal{R}_k^g(\xi), \quad (1.31)$$

$$\mathcal{L}_\theta\{\theta_k(\xi) - \mathcal{X}_k \theta_{k-1}(\xi)\} = \hbar_\theta \mathcal{R}_k^\theta(\xi), \quad (1.32)$$

$$f_k(0) = \frac{\partial f_k(0)}{\partial \xi} = 0, \quad g_k(0) = \theta_k(0) = 0, \quad (1.33)$$

$$\frac{\partial f_k}{\partial \xi}\bigg|_{\xi=\infty} = \frac{\partial^2 f_k}{\partial \xi^2}\bigg|_{\xi=\infty} = 0, \quad g_k|_{\xi=\infty} = \frac{\partial g_k}{\partial \xi}\bigg|_{\xi=\infty} = 0, \quad \theta_k|_{\xi=\infty} = 0, \quad (1.34)$$

here, $\mathcal{X}_k = \begin{cases} 0, when\ k \leq 1 \\ 1, when\ k > 1 \end{cases}$,

and

$$\mathcal{R}_k^f(\xi) = f_{k-1}''' + \sum_{m=0}^{k-1}(f_{k-1-m}f_m'' - f_{k-1-m}'f_m') + 2\lambda g_{k-1} - M f_{k-1}', \quad (1.35)$$

$$\mathcal{R}_k^g(\xi) = g_{k-1}'' + \sum_{m=0}^{k-1}(f_{k-1-m}g_m' - g_{k-1-m}f_m') - 2\lambda f_{k-1}' - M g_{k-1}, \quad (1.36)$$

$$\mathcal{R}_k^\theta(\xi) = \theta_{k-1}'' + \sum_{m=0}^{k-1}\left\{ \begin{array}{c} Pr(\theta_{k-1-m}'f_m - 2\theta_{k-1-m}f_m') \\ +PrEc\left(\begin{array}{c} f_{k-1-m}''f_m'' + g_{k-1-m}'g_m' \\ +M(f_{k-1-m}'f_m' + g_{k-1-m}g_m) \end{array} \right) \end{array} \right\}. \quad (1.37)$$

The averaged squared residuals of Eqs. (1.11)-(1.13) are defined as follows:

$$E_{f,k} = \frac{1}{20}\int_0^{20}\left\{ \mathcal{N}_f\left(\sum_{i=0}^k f_i(\xi), \sum_{i=0}^k g_i(\xi) \right) \right\}^2 d\xi, \quad (1.38)$$

$$E_{g,k} = \frac{1}{20}\int_0^{20}\left\{ \mathcal{N}_g\left(\sum_{i=0}^k f_i(\xi), \sum_{i=0}^k g_i(\xi) \right) \right\}^2 d\xi, \quad (1.39)$$

$$E_{\theta,k} = \frac{1}{20}\int_0^{20}\left\{ \mathcal{N}_\theta\left(\sum_{i=0}^k f_i(\xi), \sum_{i=0}^k \theta_i(\xi) \right) \right\}^2 d\xi. \quad (1.40)$$

The total average squared residual is determined as:

$$E_{T,k} = E_{f,k} + E_{g,k} + E_{\theta,k}. \tag{1.41}$$

The above stated procedure is implemented within BVPH 2.0, and total averaged squared residuals in some cases are presented in Figs. 1.2 (a) & 1.2(b).
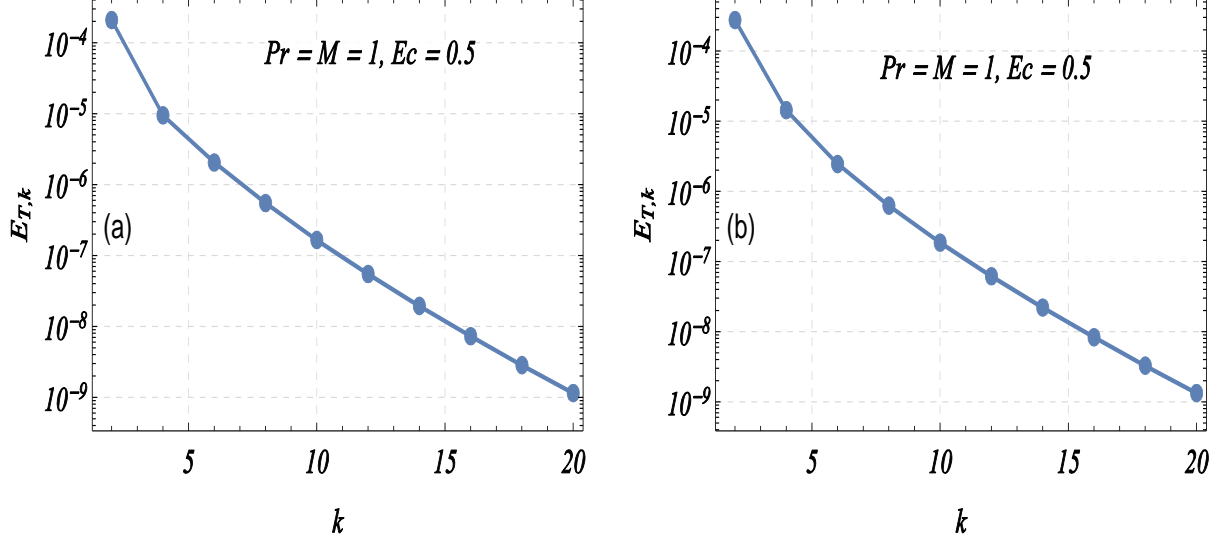
Figs. 1.2(a) &1.2(b): Graphical representation of overall averaged squared residual $E_{T,k}$ versus approximation order k for (a) $\lambda = 0$ and (b) $\lambda = 0.2$.

1.4. Viscoelastic Fluid Model

- **Walters-B fluid model**

The Walters B fluid model is developed specifically to analyze viscoelastic behavior. The stress tensor τ for Walters-B model is presented below:

$$\mathbf{S} = \mu \mathbf{A}_1 - k_0 \left\{ \frac{d\mathbf{A}_1}{dt} - \mathbf{L}\mathbf{A}_1 - \mathbf{A}_1 \mathbf{L}^t \right\}, \tag{1.42}$$

where k_0 is the material parameter of Walters-B model, p gives the pressure and the first Rivlin-Ericksen tensor is given by: $\mathbf{A}_1 = (\nabla \mathbf{V}) + (\nabla \mathbf{V})^t$.

The continuity equation, momentum equations and energy equation for a three-dimensional MHD flow of an incompressible Walters-B fluid, considering boundary layer approximations, are detailed below.

$$u_x + v_y + w_z = 0, \tag{1.43}$$

8

$$uu_x + vu_y + wu_z - 2\Omega v$$

$$= vu_{zz} + \frac{k_0}{\rho} \left\{ \begin{array}{c} 2u_{yz}v_z + 2u_zv_{yz} + 4u_{xz}u_z \\ -vu_{yzz} - uu_{xzz} - wu_{zzz} \\ +u_yv_{zz} + v_yv_{zz} + 2u_{zz}w_z + 3u_zw_{zz} \end{array} \right\} - \frac{\sigma B_0^2 u}{\rho}, \tag{1.44}$$

$$uv_x + vv_y + wv_z + 2\Omega u$$

$$= vv_{zz} + \frac{k_0}{\rho} \left\{ \begin{array}{c} 2v_{xz}u_z + 2v_zu_{xz} + 4v_{yz}v_z \\ -uv_{xzz} - vv_{yzz} - wv_{zzz} \\ +v_xu_{zz} + v_yv_{zz} + 2v_{zz}w_{z+} + 3v_zw_{zz} \end{array} \right\} - \frac{\sigma B_0 v}{\rho}, \tag{1.45}$$

$$uT_x + vT_y + wT_z = \frac{\kappa}{\rho C_p}T_{zz} - \frac{k_0}{\rho C_p} \left\{ \begin{array}{c} u(u_{xz}u_z + v_{xz}v_z) + v(u_{yz}u_z + v_{yz}v_z) \\ +w(u_{zz}u_z + v_{zz}v_z) - 3u_xu_z^2 - 3u_zv_zu_y \\ -3u_z^2w_z - 3v_xu_zv_z - 3v_yv_z^2 - 3v_z^2w_z \end{array} \right\} + \tag{1.46}$$

$$\frac{v}{C_p}(u_z^2 + v_z^2) + \frac{\sigma B_0^2}{\rho C_p}(u^2 + v^2).$$

Here, ρ is the fluid density, Ω represent the angular velocity, electrical conductivity is given by κ and C_p signifies the specific heat capacity.

- **Jeffrey fluid model**

Another important viscoelastic model is the Jeffrey model which accounts for the stress relaxation time and retardation time phenomena in a fluid motion. This fluid model effectively comprehends some non-Newtonian fluids with time scale memory effect. Stress tensor τ for the Jeffrey fluid has the following form:

$$\tau = \frac{\mu}{1 + \lambda_2}\left(\mathbf{A}_1 + \lambda_1 \frac{d\mathbf{A}_1}{dt}\right), \tag{1.47}$$

where λ_2 shows the ratio of relaxation to the retardation time while λ_1 denotes the retardation time. For a three-dimensional motion, the above equation (1.47) produces the following conservation equations under boundary layer approximations:

$$u_x + v_y + w_z = 0, \tag{1.48}$$

$$uu_x + vu_y + wu_z - 2\Omega v = \frac{v}{1 + \lambda_2}\left\{u_{zz} + \lambda_1\left(\begin{array}{c}uu_{xzz} + vu_{yzz} + wu_{zzz} \\ +u_zu_{xz} + v_zu_{yz} + w_zu_{zz}\end{array}\right)\right\} - \frac{\sigma B_0^2 u}{\rho}, \tag{1.49}$$

$$uv_x + vv_y + wv_z + 2\Omega u = \frac{v}{1 + \lambda_2}\left\{v_{zz} + \lambda_1\left(\begin{array}{c}uv_{xzz} + vv_{yzz} + wv_{zzz} \\ +u_zv_{xz} + v_zv_{yz} + w_zv_{zz}\end{array}\right)\right\} - \frac{\sigma B_0^2 v}{\rho}. \tag{1.50}$$

$$uT_x + vT_y + wT_z = \frac{\kappa}{\rho C_p} T_{zz} + \frac{\nu}{1+\lambda_2}\left[u_z^2 + v_z^2 + \lambda_1\left\{\begin{array}{l} u(u_{xz}u_z + v_{xz}v_z) \\ +v(u_{yz}u_z + v_{yz}v_z) \\ +w(u_{zz}u_z + v_{zz}v_z)\end{array}\right\}\right] +$$

$$\frac{\sigma B_0^2}{\rho C_p}(u^2 + v^2). \qquad (1.51)$$

1.5. Entropy Generation

In thermodynamics, entropy generation refers to the quantity of entropy generated due to irreversible processes in a system. It reflects the energy that is dispersed and no longer accessible to do useful work. The concept of entropy was first proposed by Rudolf Clausius in the 19th century. The idea of entropy has evolved to be an integral part of the Second principle of thermodynamics which states that the total entropy of an isolated system is either increasing or remains constant, but it never decreases. In a reversible process, entropy generation is always zero whereas there is a high rate of entropy generation in irreversible processes. The efficiency and sustainability of systems can be enhanced by minimizing entropy generation. This is a crucial idea in thermodynamics with an extensive range of applications across numerous areas such as in engineering, biomedical systems and in fluid mechanics. Power plants, Boilers, heat exchangers, solar panels, and combustion systems are some of its applications. The entropy generation analysis for the boundary layer flows has been extensively investigated by many recent authors including [1-4]. The entropy generation phenomenon for the above system is:

$$S_G = \frac{\kappa}{T_\infty^2}(T_z)^2 + \frac{\mu}{T_\infty}\{(u_z)^2 + (v_z)^2\} + \frac{\sigma B_0^2}{T_\infty}(u^2 + v^2), \qquad (1.52)$$

Eq. (1.52) in its non-dimensionalized form is given below where $N_G(\xi) = S_G T_\infty \nu / \kappa a (T_w - T_\infty)$ is entropy generation number.

$$N_G(\xi) = \alpha\theta'^2 + PrEc(f''^2 + g'^2) + PrEc(f'^2 + g^2), \qquad (1.53)$$

and $\alpha = (T_w - T_\infty) / T_\infty$ signifies temperature difference parameter.

1.6. Dimensionless numbers
1.6.1. Prandtl number

The significance of momentum diffusivity in relation to thermal diffusivity in fluid flow is represented by Prandtl number. It is expressed as:

$$Pr = \frac{\mu C_p}{\kappa},\tag{1.54}$$

in which μ represents the dynamic viscosity, C_p is the specific heat capacity and κ is the thermal conductivity.

1.6.2. Eckert number

The Eckert number signifies the relation between the flow's kinetic energy and enthalpy difference. It is utilized to analyze the heat dissipation. It is given as:

$$Ec = \frac{u^2}{C_p \Delta T},\tag{1.55}$$

where u is the average velocity, C_p shows specific heat capacity and ΔT gives the temperature difference.

1.6.3. Reynolds number

The Reynolds number, represented by Re, compares the inertial forces to viscous forces. Mathematically, one has

$$Re = \frac{vL}{v},\tag{1.56}$$

here v is the velocity, L is the characteristic length and v is the kinematic viscosity.

1.6.4. Nusselt number

The Nusselt number evaluates the relationship between convective heat transfer and conductive heat transfer. It is expressed as:

$$Nu = \frac{hL}{\kappa},\tag{1.57}$$

in which h shows convective heat transfer, L is the characteristic length and κ represents the thermal conductivity.

1.7. Literature review

Non-Newtonian fluid dynamics is one of the most prominent disciplines of applied mathematics in modern times. Non-Newtonian fluids are identified by their deviation from Newton's law of viscosity, typically exhibiting nonlinear stress-strain relationships that generally do not intersect at the origin. Non-Newtonian fluid motion is frequently witnessed in real-world applications like pharmaceutical applications, processing of polymer melts, slurry transport, wastewater treatment, coating applications, physiological processes and geophysical and oil exploration processes. Non-Newtonian fluids can be mainly categorized into three forms: shear thinning or pseudoplastic, shear thickening or dilatant and viscoelastic. Shear-thinning fluids (e.g. paints, ketchup, yogurt etc.) demonstrate a reduction in apparent viscosity as the rate of deformation rises. A fluid that exhibits shear-thickening behavior, where its viscosity increases with the shear strain rate, can be illustrated by mixtures like cornstarch in water or honey. Viscoelastic fluids, a unique subclass of non-Newtonian fluids, display both viscous and elastic properties, deforming under stress and returning to their original shape once the force is removed. Examples include polymer melts, biological fluids, hydrogels, slurries, paints etc. Due to their unique properties, viscoelastic fluids have a vast range of applications in polymer processing, food industry, the textile industry and material science. The Weissenberg effect, driven by the elastic nature of viscoelastic fluids, causes the fluid to climb up a rod when stirred, unlike Newtonian fluids which form a dip. The well-known second-grade and Walters-B models are two distinct theoretical frameworks used to describe the behavior of certain viscoelastic materials. In recent years, these models have been extensively applied to characterize viscoelastic behavior in various flow scenarios which include peristaltic flows [5-10], channel flows [11,12], flows induced by stretching sheets/cylinders [13-17] and flows developed by rotating disks [18-21].

Examining flow characteristics of molten polymers during molding process, the production of metal and plastic sheets and the creation of glass fibers are key applications involving non-Newtonian flow above a deformable boundary. Furthermore, modeling of rotating flows holds profound significance across several applications: optimizing energy transfer in turbomachinery,

understanding cyclones and hurricanes dynamics, boosting the efficiency of wind and hydroelectric turbines, enhancing industrial mixing and stirring processes and designing better aeration systems for wastewater treatment, to mention a few. Wang's intriguing work [22] explored the dynamics of fluid motion across a deforming boundary within a rotating frame. In [22], the introduction of the Coriolis force added a new parameter λ representative of the ratio between the rotation rate and the surface deformation rate. Wang [22] derived perturbation results for small values of λ and asymptotic results for large values, both of which aligned well with exact numerical integration results. Rajeswari and Nath [23] incorporated time-dependent surface stretch rate to introduce unsteadiness into Wang's formulation. Using the Keller-Box numerical scheme, the authors in [23] provided computational results for this dynamic scenario. Subsequently, Nazar et al. [24] employed the Keller-Box treatment to explore the unsteady motion across a plate undergoing sudden deformation within a rotating frame. Wang's mathematical framework is investigated using various viscoelastic models, considering different physical effects (see, for instance, [25-29])

Heat transfer refers to the transport of thermal energy from one item to another owing to temperature gradient between them. Understanding the principles of heat transfer in fluid dynamics is crucial for engineering applications like boosting heat exchangers efficiency in power plants and industrial operations, refining cooling rates in metal forming and polymer extrusion processes for achieving the desired product, developing better heating and cooling systems for buildings and enhancing cooling mechanisms in solar panels, among other applications. Moreover, viscous dissipation refers to the process in which mechanical energy alters into heat because of fluid's viscosity. The velocity gradient, fluid's viscosity and elasticity are some of parameters that determine how much heat is produced by viscous dissipation. This effect is significant and cannot be overlooked in scenarios involving high-speed or highly viscous flows. Moreover, the inclusion of stresses in viscous dissipation introduces additional terms in the energy equation when assuming viscoelastic fluid behavior, which can require efficient computational methods. For a deeper understanding of recent studies on viscous heating mechanisms in non-Newtonian flows, readers should consult the referenced papers [30-33] and the articles cited within them.

The cited literature clearly indicates a renewed interest among researchers in investigating the rotational effects on viscoelastic fluids under various physical conditions. As per authors'

information, no existing study has explored the rotational flow of Walters-B fluid and Jeffery fluid over a steadily stretching plate within a rotating frame. This thesis addresses the issue by examining the heat transport mechanism, incorporating the effects of viscous heating and Joule heating.

CHAPTER 2:

Exploring entropy production in MHD Walters-B fluid motion in a rotating frame with frictional heating using OHAM based package BVPh 2.0

Introduction

This chapter addresses the rotational flow of Walters B fluid by examining the heat transport mechanism, incorporating the effects of viscous heating and Joule heating. Furthermore, an analysis and evaluation of the entropy production expression are conducted under different considered factors. Here, the well-proven optimal analysis method (OHAM), which is included in the MATHEMATICA package BVPh 2.0, is used as the solution methodology. To verify the precision of the obtained simulations, we generated plots showing the total squared residuals in relation to the approximation order. The primary aim of this chapter is to analyze subtle physical variables like the skin friction factor and wall cooling rate under novel effects, specifically viscoelasticity, frictional heating and fluid rotation.
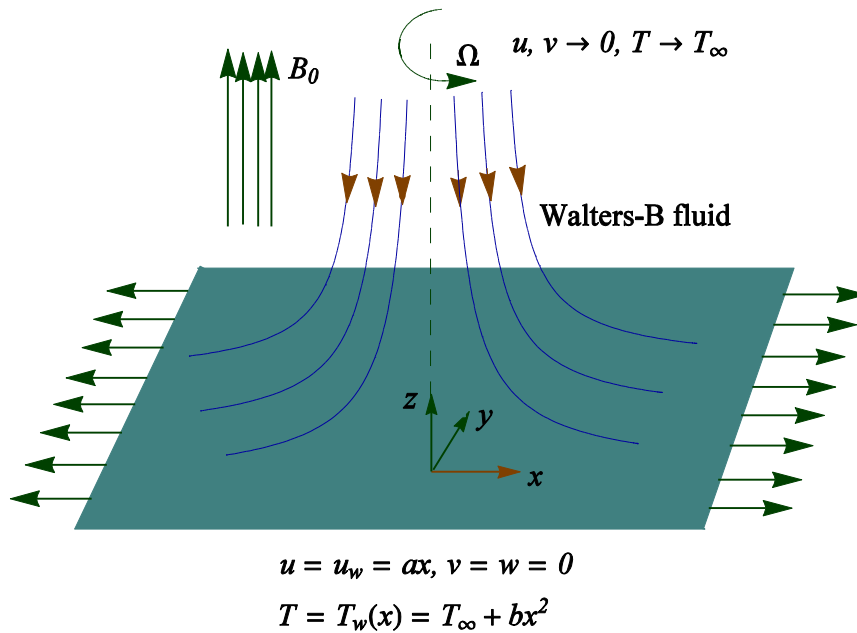

Fig. 2.1: A graphical visualization of the flow situation along with coordinate system.

2.1. Mathematical Modeling

Consider a non-Newtonian fluid—like paint, synthetic polymers like silly putty, slime etc., some food products such as cheese, yoghurt, mayonnaise etc. or polymer melts—conforming to the Walters-B model, interacting with a flat elastic surface, depicted in Fig. 2.1. The surface positioned in the $z = 0$ plane extends along the x-direction with velocity $u = ax$, where $a > 0$ is the constant. By considering a rotating frame of reference characterized by the angular velocity $\mathbf{\Omega}$, we incorporate two extra forces, Coriolis and Centrifugal, into the conservation equations. The surface is regarded to be in a non-isothermal state with temperature $T_w(x) = T_\infty + bx^2$, where T_∞ denotes the temperature's ambient value. Accounting the assumptions of incompressibility and steadiness, the flow problem translates into the following equations [29]:

$$\nabla \cdot \mathbf{V} = 0, \tag{2.1}$$

$$\rho\{(\mathbf{V} \cdot \nabla)\mathbf{V} + (2\mathbf{\Omega} \times \mathbf{V}) + \mathbf{\Omega} \times (\mathbf{\Omega} \times \mathbf{r})\} = -\nabla p + \nabla \cdot \mathbf{S} + \mathbf{J} \times \mathbf{B}, \tag{2.2}$$

$$\rho C_p\{(\mathbf{V} \cdot \nabla)T\} = \kappa \nabla^2 T + \mathbf{S} : \nabla \mathbf{V} + \sigma B_0^2 (\mathbf{V} \cdot \mathbf{V}), \tag{2.3}$$

where the fluid density is designated by ρ, while the velocity vector is indicated by $\mathbf{V}$. The angular velocity vector is given by $\mathbf{\Omega}$, current density is denoted by $\mathbf{J}$, magnetic field strength is symbolized by $\mathbf{B}$, electrical conductivity is represented by κ and specific heat capacity is referred to as C_p.

For visco-elastic fluids, Beard and Walters [34] suggested the following stress tensor:

$$\mathbf{S} = \mu \mathbf{A}_1 - k_0 \left\{ \frac{d\mathbf{A}_1}{dt} - \mathbf{L}\mathbf{A}_1 - \mathbf{A}_1 \mathbf{L}^t \right\}. \tag{2.4}$$

The dynamic viscosity is represented by μ and the first Rivlin-Ericksen tensor is given by: $\mathbf{A}_1 = (\nabla V) + (\nabla \mathbf{V})^t$.

By applying the stress tensor components from Eq. (2.4), and considering the boundary layer assumptions, Eqs. (2.1)-(2.3) become:

$$u_x + v_y + w_z = 0, \tag{2.5}$$

$$uu_x + vu_y + wu_z - 2\Omega v$$
$$= vu_{zz} + \frac{k_0}{\rho} \left\{ \begin{array}{c} 2u_{yz}v_z + 2u_z v_{yz} + 4u_{xz}u_z \\ -vu_{yzz} - uu_{xzz} - wu_{zzz} \\ +u_y v_{zz} + v_y v_{zz} + 2u_{zz}w_z + 3u_z w_{zz} \end{array} \right\} - \frac{\sigma B_0^2 u}{\rho}, \tag{2.6}$$

16

$$uv_x + vv_y + wv_z + 2\Omega u$$

$$= vv_{zz} + \frac{k_0}{\rho} \left\{ \begin{array}{c} 2v_{xz}u_z + 2v_z u_{xz} + 4v_{yz}v_z \\ -uv_{xzz} - vv_{yzz} - wv_{zzz} \\ +v_x u_{zz} + v_y v_{zz} + 2v_{zz}w_{z+} + 3v_z w_{zz} \end{array} \right\} - \frac{\sigma B_0 v}{\rho}, \tag{2.7}$$

$$uT_x + vT_y + wT_z = \frac{\kappa}{\rho C_p} T_{zz} - \frac{k_0}{\rho C_p} \left\{ \begin{array}{c} u(u_{xz}u_z + v_{xz}v_z) + v(u_{yz}u_z + v_{yz}v_z) \\ +w(u_{zz}u_z + v_{zz}v_z) - 3u_x u_z^2 - 3u_z v_z u_y \\ -3u_z^2 w_z - 3v_x u_z v_z - 3v_y v_z^2 - 3v_z^2 w_z \end{array} \right\} + \tag{2.8}$$

$$\frac{v}{C_p}(u_z^2 + v_z^2) + \frac{\sigma B_0^2}{\rho C_p}(u^2 + v^2).$$

The following boundary conditions will be invoked to solve the 2 equations:

$$u = u_w(x) = ax, \quad v = 0, \quad w = 0, \quad T = T_w(x) \text{ at } z = 0, \tag{2.9}$$

$$u \to 0, \quad u_z \to 0, \quad v \to 0, \quad v_z \to 0, \quad T \to T_\infty \text{ as } z \to \infty. \tag{2.10}$$

Choosing the transformations:

$$u = axf'(\xi), \quad v = axg(\xi), \quad w = -f(\xi)\sqrt{av}, \quad \theta(\xi) = \frac{T - T_\infty}{T_w - T_\infty}, \tag{2.11}$$

in which $\xi = z(a/v)^{1/2}$ is indicating similarity variable, $f(\xi)$ indicates the non-dimensional form of stream function whereas $\theta(\xi)$ defines the non-dimensional temperature, Eq. (2.5) is inherently satisfied, while Eqs. (2.6)-(2.8) are recast as follows:

$$f''' + K(f''^2 - 2f'f''' + ff^{iv}) - f'^2 + ff'' + 2\lambda g - Mf' = 0, \tag{2.12}$$

$$g'' + K(f''g' - 3f'g'' + gf''' + fg''') - f'g + fg' - 2\lambda f' - Mg = 0, \tag{2.13}$$

$$\theta'' + Pr(\theta'f - 2\theta f') +$$

$$PrEc \left\{ \begin{array}{c} -K(f'f''^2 + 4f'g'^2 - ff''f''' - fg'g'' - 3f''gg') \\ +f''^2 + g'^2 + M(f'^2 + g^2) \end{array} \right\} = 0. \tag{2.14}$$

Eq. (2.11) converts the boundary conditions (2.9) and (2.10) as below:

$$f = 0, \quad g = 0, \quad f' = 1, \quad \theta = 1 \quad \text{at} \quad \xi = 0, \tag{2.15}$$

$$f' \to 0, \quad f'' \to 0, \quad g \to 0, \quad g' \to 0, \quad \theta \to 0 \quad \text{as} \quad \xi \to \infty. \tag{2.16}$$

Eqs. (2.12)-(2.14) encompass the following parameters:

- Pr represents the Prandtl number, calculated as $Pr = \mu C_p/\kappa$.
- $M = \sigma B_0^2/\rho a$ is mentioned as magnetic field parameter.

- $K = k_0 a/\mu$ is proportionate with the material parameter k_0 and is thus identified as the elasticity parameter.

- $\lambda = \Omega/a$ is associated with the angular velocity Ω and is consequently termed the rotation parameter.

- Ec signifies the Eckert number, defined as $Ec = a^2/C_p b$.

The engineering entities of significance encompass the skin friction coefficients, C_{fx} and C_{fy}, as well as the local Nusselt number, Nu_x. These quantities are characterized by the following expressions:

$$C_{fx} = \frac{\tau_{zx}|_{z=0}}{\rho u_s^2}, \quad C_{fy} = \frac{\tau_{zy}|_{z=0}}{\rho u_w^2}, \quad Nu_x = \frac{xq_w}{k(T_w - T_\infty)}, \tag{2.17}$$

in which the stresses τ_{zx} and τ_{zy}, can be evaluated from Eq. (2.4):

$$\tau_{zx} = \mu(u_z) - k_0(uu_{xz} + vu_{yz} + wu_{zz} - u_x u_z - u_y v_z - 3u_z w_z), \tag{2.18}$$

$$\tau_{zy} = \mu(v_z) - k_0(uv_{xz} + vv_{yz} + wv_{zz} - v_y v_z - v_x u_z - 3v_z w_z), \tag{2.19}$$

and $q_w = -k(\partial T/\partial z)$ denotes the heat flux through the wall. It can be verified that the quantities in Eq. Using Eq. (2.11), one can derive the following forms of the quantities in Eq. (2.17):

$$Re_x^{\frac{1}{2}} C_{fx} = (1 - 3K)f''(0), \quad Re_x^{\frac{1}{2}} C_{fy} = (1 - 4K)g'(0), \quad Re_x^{-\frac{1}{2}} Nu_x = -\theta'(0), \tag{2.20}$$

where $Re_x^{\frac{1}{2}} = u_w x/v$ is expressing the local Reynold's number.

2.1.1. Special case of Newtonian fluid flow

Eqs. (2.12) through (2.16) collapse to the viscous flow situation when $K = 0$ is substituted. The following system is pertinent in this scenario:

$$f''' - f'^2 + ff'' + 2\lambda g - Mf' = 0, \tag{2.21}$$

$$g'' - f'g + fg' - 2\lambda f' - Mg = 0, \tag{2.22}$$

$$\theta'' + Pr(\theta'f - 2\theta f') + PrEc(f''^2 + g'^2) + MPrEc(f'^2 + g^2) = 0, \tag{2.23}$$

along with the same conditions (2.15) and (2.16).

2.2. Assessment of entropy creation

Entropy rise quantifies the irreversibility and efficiency loss in mechanical systems, occurring because of heat transfer and frictional heating effects. Therefore, shear stresses and temperature gradients are responsible for entropy formation within boundary layer flows. Mathematically, the entropy generation rate S_G is defined as follows:

$$S_G = \frac{\kappa}{T_\infty^2}(T_z)^2 + \frac{\mu}{T_\infty}\{(u_z)^2 + (v_z)^2\}$$

$$- \frac{k_0}{T_\infty}\begin{Bmatrix} u(u_{xz}u_z + v_{xz}v_z) + v(u_{yz}u_z + v_{yz}v_z) + \\ w(u_{zz}u_z + v_{zz}v_z) - 3u_x u_z^2 - 3u_z u_y v_z - \\ 3v_x u_z v_z - 3v_y v_z^2 - 3v_z^2 w_z \end{Bmatrix} + \frac{\sigma B_0^2}{T_\infty}(u^2 + v^2), \tag{2.24}$$

The first term represents the local entropy formation occurring because of heat transport through finite temperature gradient. The second and third terms correspond to local entropy production because of viscous dissipation and the final term accounts for the impact of Joule heating.

Defining the entropy generation number as $N_G(\xi) = S_G T_\infty \nu / \kappa a (T_w - T_\infty)$, the similarity transformations (2.11) are used to obtain the following result:

$$N_G(\xi) = \alpha\theta'^2 + PrEc(f''^2 + g'^2) - PrEcK(f' f''^2 + 4f'g'^2 - ff''f''' - fg'g'' - \\ 3f''gg') + MPrEc(f'^2 + g^2), \tag{2.25}$$

where $\alpha = (T_w - T_\infty)/T_\infty$ measures the temperature difference.

Bejan number: Bejan number gives the ratio between the irreversibility owing to heat transfer and the total irreversibility within a system. It is therefore crucial for evaluating the effectiveness of heat transmission. The Bejan number is defined below:

$$Be = \frac{Entropy\ formation\ as\ a\ consequence\ of\ heat\ transfer}{Total\ entropy\ creation} \tag{2.26}$$

Using Eq. (2.25), Eq. (2.26) attains the following form:

$$Be = \frac{\alpha\theta'^2}{\alpha\theta'^2 + PrEc(f''^2 + g'^2) - PrEcK\left(f'f''^2 + 4f'g'^2 - ff''f''' - fg'g'' - 3f''gg'\right) + PrEc(f'^2 + g^2)}. \tag{2.27}$$

It is obvious from above equation that $0 < Be < 1$. When $Be = 0$, the irreversibility effects due to viscous and Joule heating effects dominate the heat transfer irreversibility. For $Be = 1/2$, both viscous heating and heat transfer effects contribute equally to the entropy rise.

2.3. Optimal homotopy analysis method (OHAM)

Homotopy analysis approach, founded by Liao [35], is known for handling a variety of non-linear problems. In 2010, Liao [36] pioneered an optimal homotopy technique, which generates approximate solutions by identifying the best possible auxiliary parameters, thereby minimizing the problem's least squared residual.

The following base functions are selected, taking into consideration the constraints (2.15) and (2.16):

$$\xi^q \exp(-m\xi); \quad q, m \geq 0 \tag{2.28}$$

To construct zeroth-order deformation problems, we specify the linear operators and initial guesses by examining the governing equations and boundary constraints, as follows:

$$\mathcal{L}_f(\varphi) = \varphi''' - \varphi', \ \mathcal{L}_g(\varphi) = \varphi'' - \varphi \ , \ \mathcal{L}_\theta(\varphi) = \varphi'' - \varphi, \tag{2.29}$$

$$f_0(\xi) = 1 - e^{-\xi}, \ g_0(\xi) = 0, \ \theta_0(\xi) = e^{-\xi}, \tag{2.30}$$

The associated non-linear operators are chosen as follows:

$$\mathcal{N}_f[f(\xi), g(\xi)] = f''' - f'^2 + ff'' + 2\lambda g - Mf' + K(f''^2 - 2f'f''' + ff^{iv}), \tag{2.31}$$

$$\mathcal{N}_g[f(\xi), g(\xi)] = g'' - f'g + fg' - 2\lambda f' - Mg + K(f''g' - 3f'g'' + gf''' + fg'''), \tag{2.32}$$

$$\mathcal{N}_\theta[f(\xi), \theta(\xi)] = \theta'' + Pr(\theta'f - 2\theta f') + PrEc[f''^2 + g'^2 - K(f'f''^2 + 4f'g'^2 - ff''f''' - fg'g'' - 3f''gg')] + MPrEc(f'^2 + g^2). \tag{2.33}$$

Utilizing the non-linear operators outlined in Eqs. (2.34)-(2.36), we compute the average squared residuals over the interval [0, 20]:

$$E_{f,k} = \frac{1}{20} \int_0^{20} \left(\mathcal{N}_f[f(\xi), g(\xi)]\right)^2 d\xi, \tag{2.34}$$

$$E_{g,k} = \frac{1}{20} \int_0^{20} \left(\mathcal{N}_g[f(\xi), g(\xi)]\right)^2 d\xi, \tag{2.35}$$

$$E_{\theta,k} = \frac{1}{20} \int_0^{20} (\mathcal{N}_\theta[f(\xi), \theta(\xi)])^2 \, d\xi. \tag{2.36}$$

The overall residual is thus evaluated from the following formula:

$$E_{T,k} = E_{f,k} + E_{g,k} + E_{\theta,k}. \tag{2.37}$$

MATHEMATICA's "BVPH 2.0" solver is applied to evaluate the series solutions. The best possible auxiliary parameters—those for which the total squared residual is lowest—are automatically determined by this solver.

2.4. Computational results and discussion

Using the analytical solutions from the method described in the preceding section, graphical results are produced for different control parameters. For a range of elastico-viscous parameter K values, graphical representations of the overall squared residual $E_{T,k}$ are shown against k, the approximation order. These graphs (Figs. 2.2(a) to 2.2(d)) illustrate a significant decline in $E_{T,k}$ with the increase in OHAM approximation order, thereby demonstrating the series solutions' convergence. The computational data also shows inverse correlations between $E_{T,k}$ and the parameters K and λ. It is concluded that for $M = 1, Pr = 1, and \, Ec = 0.5$, 15th-order series solutions are sufficiently accurate for ranges of K and λ in 0-0.5. Higher order approximations for the solutions would be necessary for K and λ values beyond this range.

Table 2.1 showcases the computational results for the skin friction factor $C_{fx}Re_x^{\frac{1}{2}}$, $C_{fy}Re_x^{\frac{1}{2}}$ across various values of K, λ and M and table 2.2 shows the local Nusselt number $Re_x^{\frac{1}{2}}Nu_x$ values for different values of K, λ, M and Ec. Notably, a higher elasticity parameter provides a considerable decay in the surface drag coefficient. An elastico-viscous fluid has a lower drag coefficient compared to a standard Newtonian fluid. The replacement of Newtonian fluid with the viscoelastic one also results in a decline in the local Nusselt number Nu_x, which measures the surface cooling rate. Moreover, as the fluid's rotational velocity increases, the stretching wall demands a greater force. Conversely, when the fluid's rotational or angular velocity increases, the surface's cooling rate decreases noticeably. Increase in magnitude of magnetic field parameter leads to an increase in skin friction coefficient. This happens due to the retarding impact of Lorentz force which

21

produces higher the velocity gradient at the surface. Similarly, it decreases the convective heat transfer's effectiveness in contrast to conduction.

Figs. 2.3(a) through 2.3(c) display visual depictions of the velocity fields f', g and f, each corresponding to various values of the elasticity parameter K. For higher values of K, the u-velocity profile (denoted as f') diminishes over a shorter vertical range, suggesting that the depth of momentum penetration is inversely related to the parameter K. The negative value of g is representative of fluid motion towards the negative y-direction. The source of this y-direction flow is the rotating frame of reference. The impact of parameter K on the vertical flow is next demonstrated through Fig. 2.3(c). The vertical flow is reduced due to decelerated horizontal flow caused by increasing K-values. With increasing K, the θ-profile shifts away from the boundary, suggesting an expansion of the thermal layer thickness or weakening of heat convection effect, a phenomenon resulting from the slowed vertical motion due to the enhanced K (see Fig. 2.3(d)).

At various values of parameter λ, which specifies the intensity of the Coriolis force, the similarity profiles f', g, f and θ are next illustrated in Figs. 2.4(a) through 2.4(d). Because the parameter λ gives the ratio between rotation and stretch rates, increasing it is therefore expected to slow down the stretching surface driven flow in the x-direction, as noticed through Fig. 2.4(a). Furthermore, for the satisfaction of mass conservation constraint, the vertical flow is accordingly reduced. It may be noted that while the parameter λ affects the boundary layer in a similar manner to K, increasing K has a greater impact on the velocity components variation than altering λ. As the rotational speed increases, the y-direction flow produced by the fluid's rotation is naturally expected to accelerate, as shown in Fig. 2.4(b). Increasing λ considerably reduces the heat convection effect due to the decreased f, which boosts heat conduction and causes the thermal boundary layer to progress, as seen in Fig. 2.4(d).

In Figs. 2.5(a) through 2.5(d), the Lorentz force behavior on the rotating viscoelastic fluid over a deforming plate is demonstrated. It is anticipated that the flow created by the deforming wall will be resisted by the magnetic field acting normal to the surface. That is why, with increasing M, the velocity curves depicted in Figs. 2.5(a)-2.5(d) reach far-field conditions at reduced vertical distances. The resistive behavior of the Lorentz force as a result of the magnetic field consideration is indicated by the decrease in velocity distributions with rising M-values. Here, we shall discuss

a fascinating phenomenon called Joule heating, which is based on the fundamental notion that heat is released as electric current flows through a conductor due to its resistance. As M increases, more heat is produced as a result of the Joule heating factor in Eq. (2.8), improving the thermal layer thickness (see Fig. 2.5(d)).

By altering the values of Pr, the Prandtl number, Fig. 2.6 demonstrates how the temperature curve varies. Because liquids have a higher viscosity to heat conductivity ratio than gases, Pr is chosen higher for liquids (Pr>=1). Given the inverse relationship between Pr and thermal conductivity, it is anticipated that a growth in Pr will result in a decrement in temperature profile, as seen in Fig. 2.6. As Pr enlarges, heat convection effect represented by the term $Pr(f\theta' - 2f'\theta)$ increases, enhancing the cooling rate at the boundary.

Fig. 2.7 illustrates the temperature profiles across various Eckert numbers through a graphical representation. The Eckert number, which compares the kinetic energy with enthalpy, is significant when dealing with highly viscous fluids or high-speed flows. A rise in Eckert number contributes to the translation of kinetic energy into internal energy as a result of the work done against the fluid's viscous forces. As the Eckert number increases, the boundary layer generates more heat, leading to an elevated temperature profile.

Graphical visualizations of skin friction factor and local Nusselt number as functions of rotation parameter λ are provided at different elasticity parameters in the Figs. 2.8 and 2.9 respectively. Firstly, parameter K has a significantly stronger influence on the required surface force compared to parameter λ. Secondly, by raising the elasticity parameter K, the dominance of viscous forces is subdued resulting in a reduced skin friction coefficient. When we increase the values of the elasticity parameter, the convection phenomenon becomes prominent, resulting in an elevated local Nusselt number.

Figs. 2.10(a) and 2.10(b) illustrate how the entropy generation number varies across the boundary layer as the temperature difference parameter (α) and the elasticity parameter (K) change. A significant increase in entropy generation occurs as the temperature gradient becomes steeper. Conversely, increasing the elasticity parameter results in a reduction in entropy production. From a physical perspective, raising the material parameter k_0 reduces the contribution of viscous heating towards entropy production resulting in a lower entropy generation number N_G.

23

To compare the irreversibility effects due to heat transfer and frictional heating, we generate Bejan number profiles for changing values of α and K in the Figs. 2.11(a) and 2.11(b) respectively. The Bejan number is lower near the wall where temperature is higher, and it converges to unity outside the boundary layer. It suggests that irreversibility effects due to frictional heating are prominent near the wall and vanish as $\xi \to \infty$. We noticed a direct correlation between the Bejan number with both parameters: α and K.
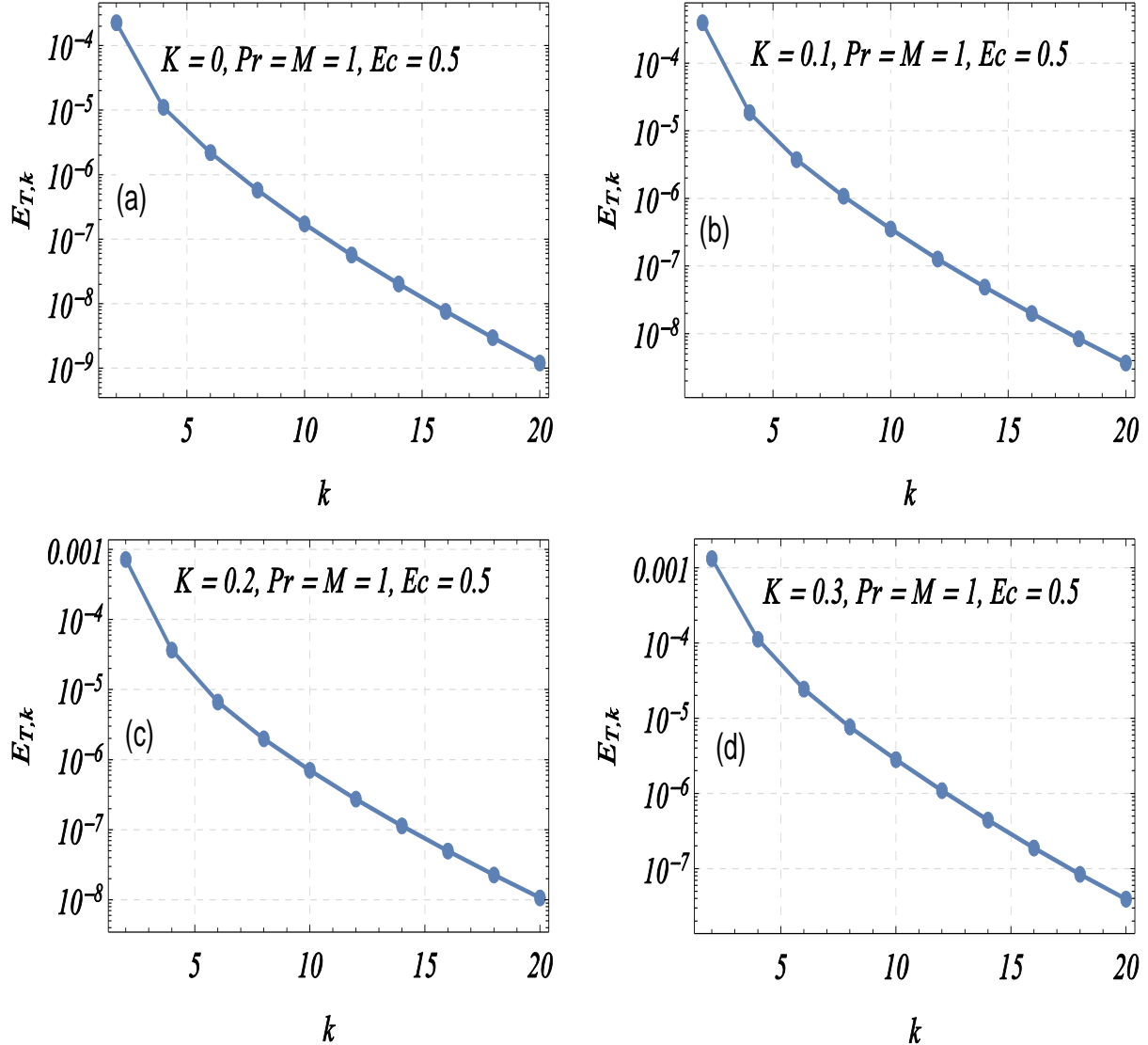
Figs. 2.2(a)-2.2(d): Graphical representation of overall averaged squared residual $E_{T,k}$ versus approximation Order k for various elasticity parameter K-values when $\lambda = 0.1$.

Table 2.1: Analysis of skin friction variations with rotation parameter λ, elasticity parameter K and magnetic interaction parameter M for given conditions: $Pr = 1$ and $Ec = 0.5$.

λ	K	M	$(1-3K)f''(0)$	$(1-4K)g'(0)$
0.1	0.2	1	-0.63343	-0.02524
0.2			-0.63631	-0.05019
0.25			-0.63842	-0.06248
0.3			-0.64093	-0.07459
0.4			-0.64708	-0.09824
0.1	0.1	1	-1.04514	-0.05667
	0.2		-0.63343	-0.02524
	0.3		-0.16931	0.04418
	0.4		0.36736	0.58456
	0.5		1.00023	0.19514
0.1	0.1	0.5	-0.90650	-0.06793
		0.75	-0.97819	-0.06154
		1	-1.04514	-0.05667
		1.25	-1.10813	-0.05281
		1.5	-1.16777	-0.04965

Table 2.2: Analysis of local Nusselt number variations with rotation parameter λ, elasticity parameter K, magnetic interaction parameter M and Eckert number Ec for given condition: $Pr = 1$.

| λ	K	M	Ec	$-\theta'(0)$
0.1	0.2	1	0.5	0.79261
0.2				0.78263
0.25				0.77530
0.3				0.76650
0.4				0.74486
0.1	0.1	1	0.5	0.80249
	0.2			0.79261
	0.3			0.78000
	0.4			0.76626
	0.5			0.74019
0.1	0.1	0.5	0.5	1.00466
		0.75		0.87869
		1		0.80249
		1.25		0.73108
		1.5		0.66377
0.1	0.1	1	0.25	0.99788
			0.5	0.80249
			1	0.41136
			1.5	0.02094
			2	0.36955
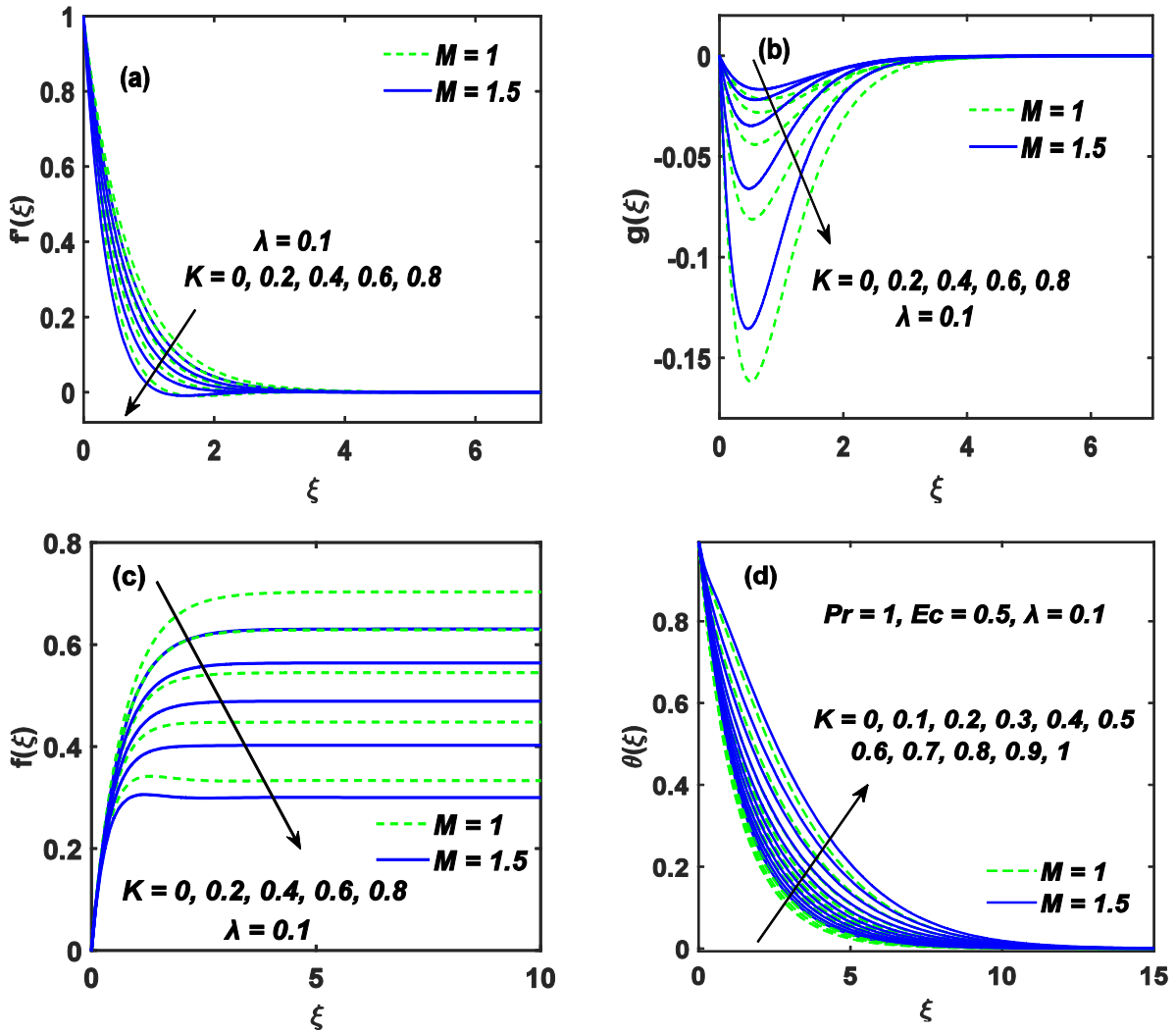
Figs. 2.3(a)-2.3(d): Impact of Elasticity parameter K variation on the velocities (f', g and f) and temperature (θ) patterns.
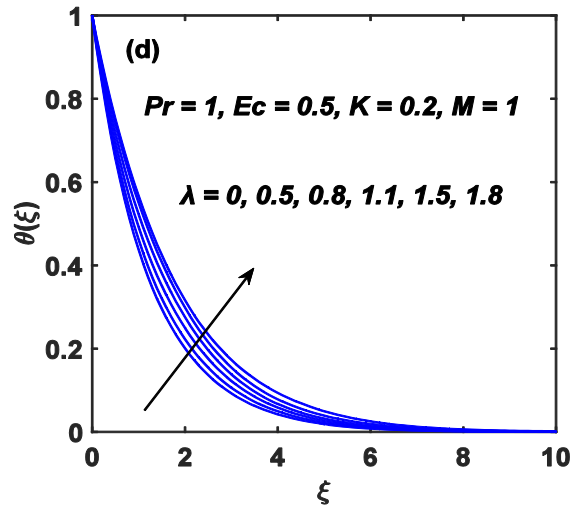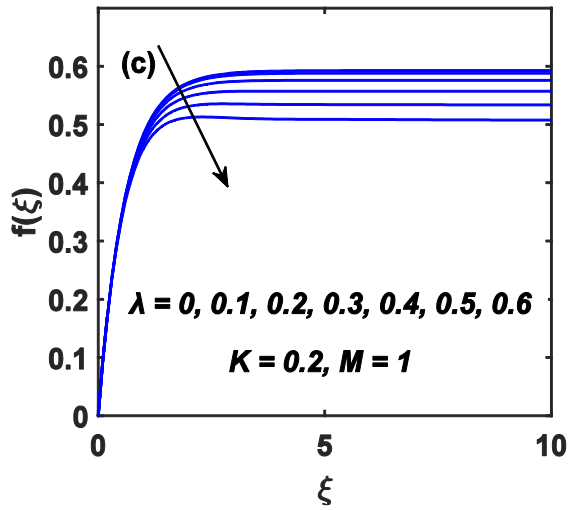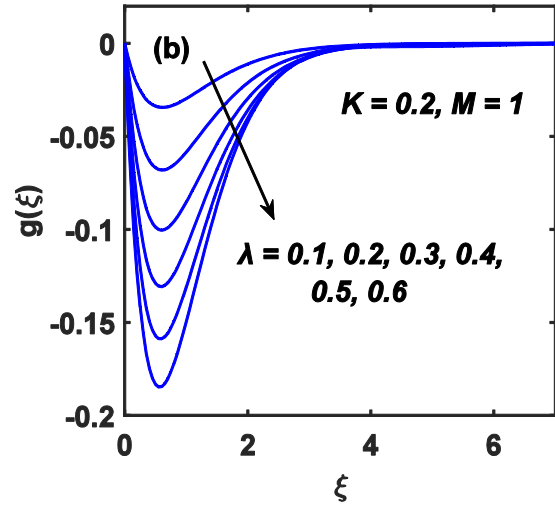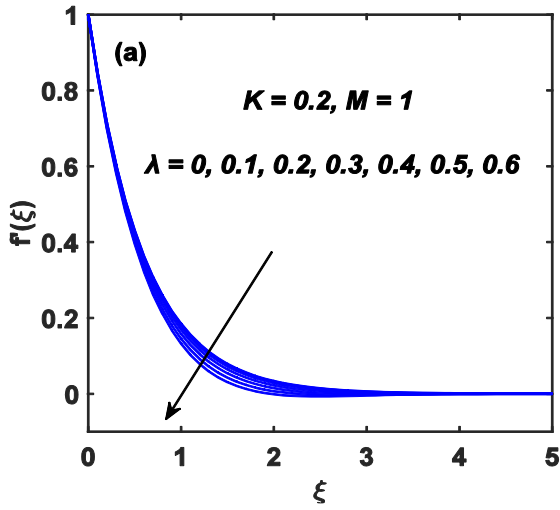
Figs. 2.4(a)-2.4(d): Impact of rotation parameter λ variation on the velocities (f', g and f) and temperature (θ) patterns.
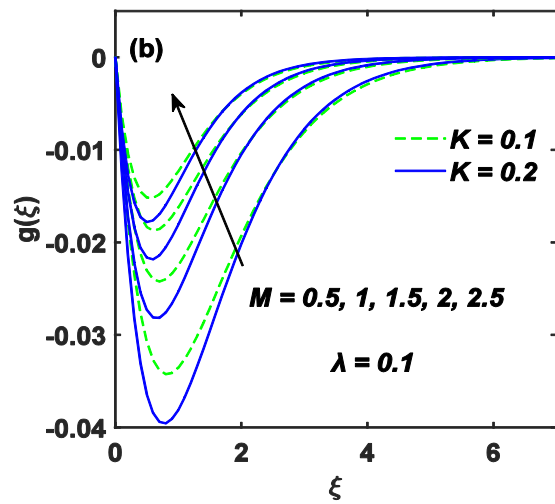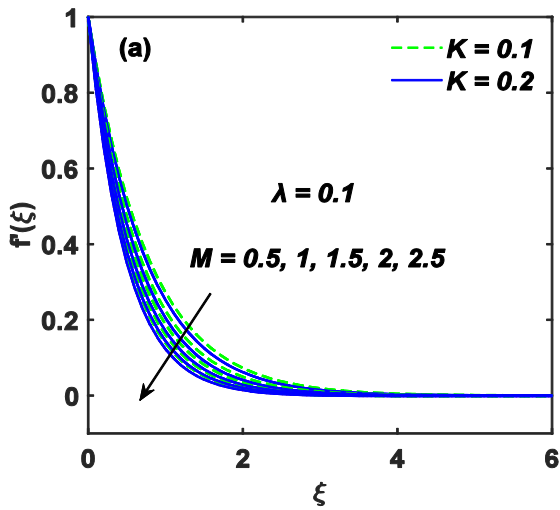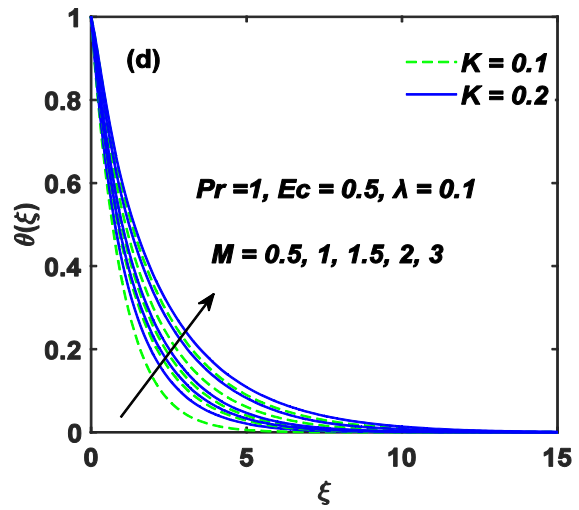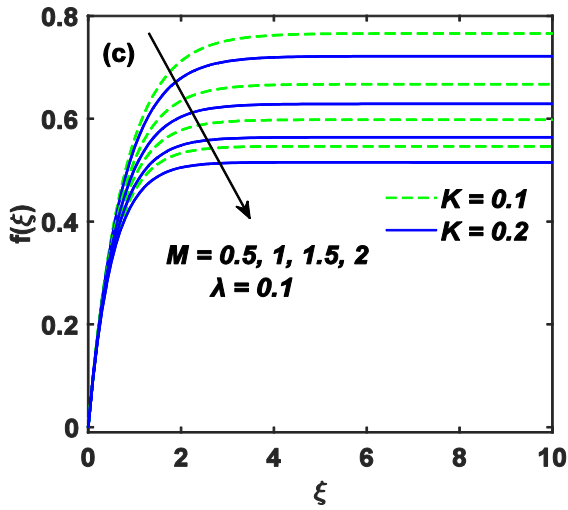
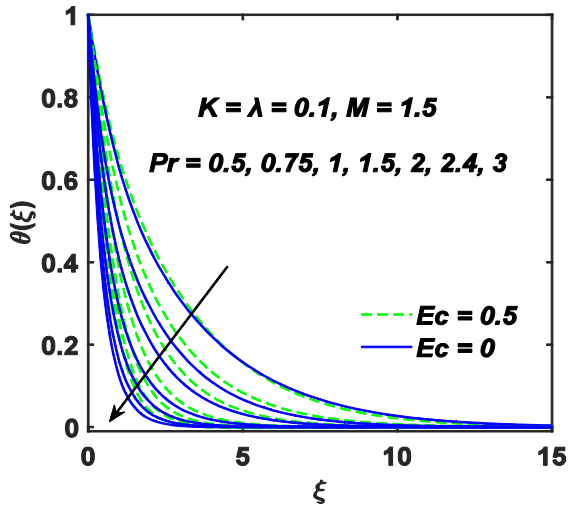Figs. 2.5(a)-2.5(d): Behavior of magnetic influence parameter M variation on the velocities (f', g and f) and temperature (θ) patterns.

Fig. 2.6: Impacts of Prandtl number Pr on the temperature (θ) dynamics.
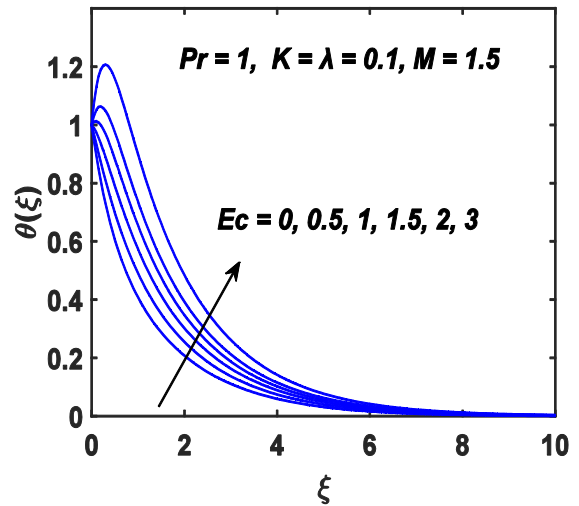
Fig. 2.7: Impacts of Ecker number Ec on the temperature (θ) dynamics.
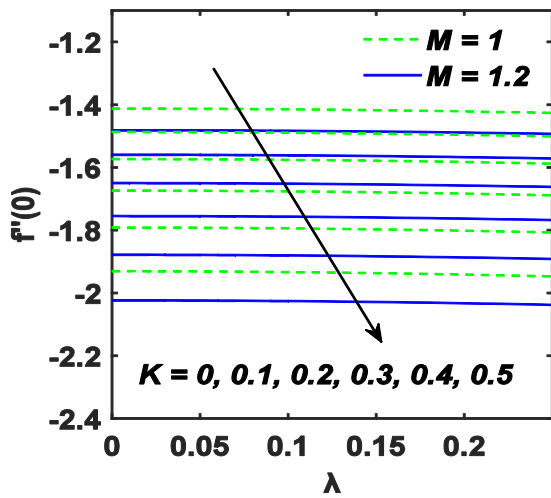
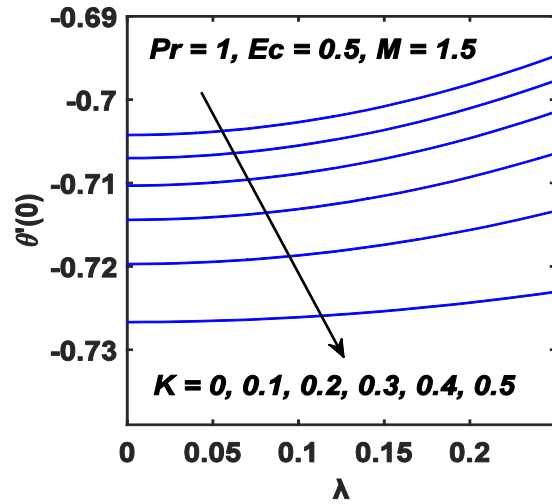Fig. 2.8: Impact of elasticity parameter K variation on the skin friction factor.
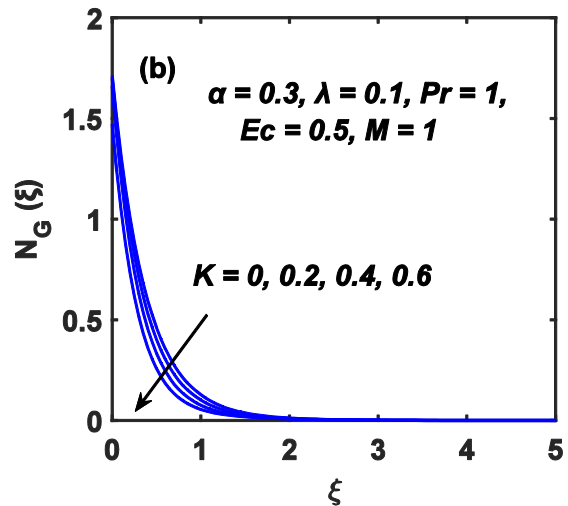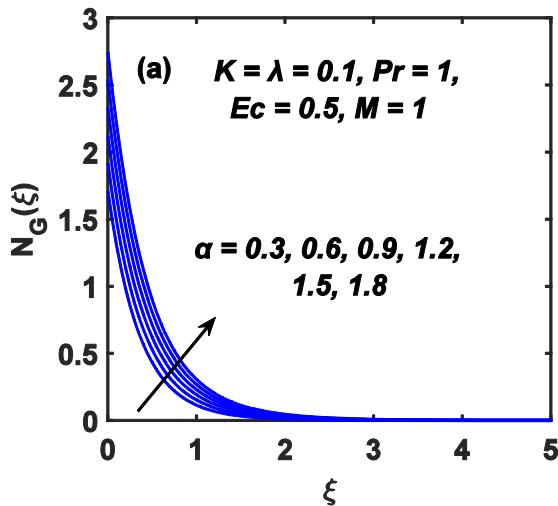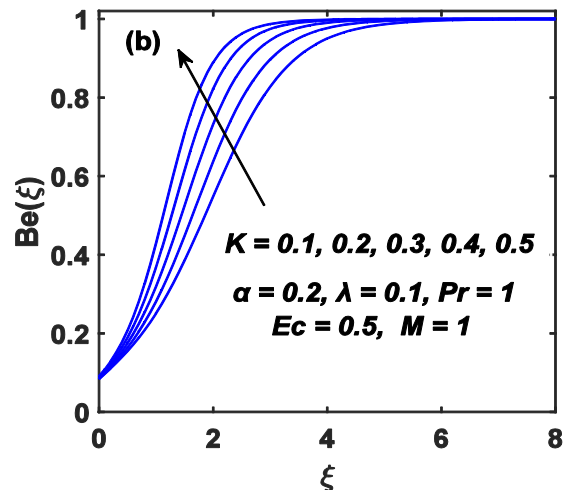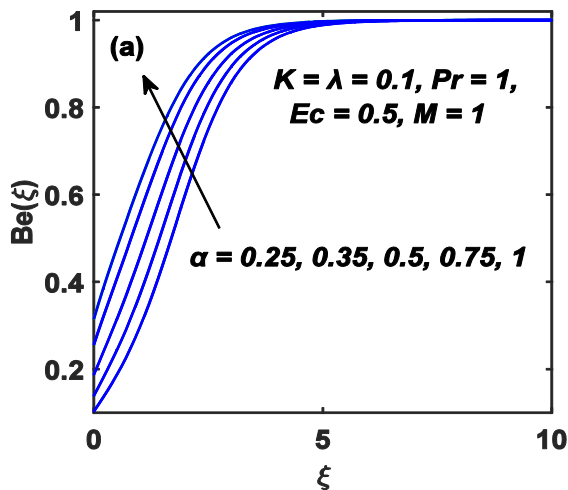

Fig. 2.9: Impact of elasticity parameter K variation on the local Nusselt number.

Figs. 2.10(a) & 2.10(b): Influence of temperature difference parameter α and elasticity parameter K on the entropy formation assessment.

Figs. 2.11(a) & 2.11(b): Influence of temperature difference parameter α and elasticity parameter K on the Bejan number.

CHAPTER 3

Entropy formation analysis for rotating flow of Jeffery fluid over a stretching surface

Introduction

This chapter analyzes the behavior of boundary layer flow of Jeffery fluid in three dimensions. We examine the effects of rotation, magnetic field and viscous dissipation on the deforming surface we have considered. By utilizing the MATHEMATICA's "BVPH 2.0", we have obtained the numerical results. The acquired results are depicted through the graphical results.

3.1. Problem formulation

We investigate the three-dimensional rotational flow of Jeffery fluid induced by a stretching surface. We adopt Cartesian coordinates in which a surface is in xy- plane and viscoelastic fluid is restricted in the space $z \geq 0$. In the x-direction, the surface is expected to deform linearly with velocity $u = cx$, where $c > 0$, is constant. Moreover, fluid experiences rotation along the z- axis with constant angular velocity $\mathbf{\Omega}$. The surface temperature is $T_w = T_\infty + bx^2$, here T_∞ signifies the fluid's ambient temperature. The stress tensor for Jeffery fluid model [37] is expressed as:

$$\tau = \frac{\mu}{1 + \lambda_2}\left(\mathbf{A}_1 + \lambda_1 \frac{d\mathbf{A}_1}{dt}\right),\tag{3.1}$$

where μ is the dynamic viscosity, λ_2 represents the ratio of relaxation to retardation time, λ_1 shows retardation time and $\mathbf{A}_1 = (\nabla \mathbf{V}) + (\nabla V)^t$ signifies the Rivlin-Ericksen tensor, while $\mathbf{V}$ represents the velocity vector. Under the assumption of steady and incompressible flow, the problem is characterized by the following equations by taking the boundary layer assumption into account:

$$u_x + v_y + w_z = 0,\tag{3.2}$$

$$uu_x + vu_y + wu_z - 2\Omega v = \frac{\nu}{1 + \lambda_2}\left\{u_{zz} + \lambda_1 \begin{pmatrix} uu_{xzz} + vu_{yzz} \\ +wu_{zzz} + u_z u_{xz} \\ +v_z u_{yz} + w_z u_{zz} \end{pmatrix}\right\} - \frac{\sigma B_0^2 u}{\rho},\tag{3.3}$$

$$uv_x + vv_y + wv_z + 2\Omega u = \frac{\nu}{1 + \lambda_2}\left\{v_{zz} + \lambda_1 \begin{pmatrix} uv_{xzz} + vv_{yzz} \\ +wv_{zzz} + u_z v_{xz} \\ +v_z v_{yz} + w_z v_{zz} \end{pmatrix}\right\} - \frac{\sigma B_0^2 v}{\rho},\tag{3.4}$$

$$uT_x + vT_y + wT_z = \frac{\kappa}{\rho C_p}T_{zz} + \frac{\nu}{1+\lambda_2}\left[u_z^2 + v_z^2 + \lambda_1\left\{\begin{array}{l}u(u_{xz}u_z + v_{xz}v_z)\\+v(u_{yz}u_z + v_{yz}v_z)\\+w(u_{zz}u_z + v_{zz}v_z)\end{array}\right\}\right] +$$

$$\frac{\sigma B_0^2}{\rho C_p}(u^2 + v^2). \qquad (3.5)$$

here ρ is the fluid density, the angular velocity vector is indicated by $\mathbf{\Omega}$, magnetic field strength is shown by $\mathbf{B}$, thermal conductivity is given by κ and C_p is referred to as specific heat capacity.

These equations will be solved by applying the following boundary conditions:

$$u = u_w(x) = cx, \quad v = 0, \quad w = 0, \quad T = T_w(x) \ at \ z = 0, \qquad (3.6)$$

$$u \to 0, \quad u_z \to 0, \quad v \to 0, \quad v_z \to 0, \quad T \to T_\infty \ as \ z \to \infty. \qquad (3.7)$$

using the following transformation:

$$u = cxf'(\xi), \quad v = cxg(\xi), \quad w = -f(\xi)(av)^{1/2}, \quad \theta(\xi) = \frac{T - T_\infty}{T_w - T_\infty}, \qquad (3.8)$$

where $\xi = z(c/v)^{1/2}$ signifies the similarity variable, $f(\xi)$ and $\theta(\xi)$ representing the non-dimensionalized form of stream function and temperature respectively. Eq. (3.2) is satisfied identically and Eqs. (3.3)-(3.5) are transformed as given below:

$$f''' + (1 + \lambda_2)(ff'' - f'^2 + 2\lambda g) + \beta(f''^2 - ff^{iv}) - (1 + \lambda_2)Mf' = 0, \qquad (3.9)$$

$$g'' + (1 + \lambda_2)(fg' - f'g - 2\lambda f') + \beta(f''g' - fg''') - (1 + \lambda_2)Mg = 0, \qquad (3.10)$$

$$(1 + \lambda_2)\theta'' + (1 + \lambda_2)Pr(f\theta' - 2\theta f') + PrEc\{f''^2 + g'^2 + \beta(f'f''^2 + f'g'^2 -$$
$$ff''f''' - fg'g'') + M(1 + \lambda_2)(f'^2 + g^2)\} = 0. \qquad (3.11)$$

The boundary conditions Eqs. (3.6)-(3.7) are transformed by using Eq.(3.8) as follows:

$$f(0) = g(0) = 0, f'(0) = \theta(0) = 1, \qquad (3.12)$$

$$f'(\infty) \to 0, f''(\infty) \to 0, g(\infty) \to 0, g'(\infty) \to 0, \theta(\infty) \to 0. \qquad (3.13)$$

The following parameters are included in Eqs. (3.9)-(3.10):

- $\lambda = \Omega/c$ is the rotation parameter corresponds to angular velocity Ω.
- $\beta = \lambda_1 c$ represents the Deborah number associated with retardation time.

33

- $M = \sigma B_0^2 / \rho c$ gives magnetic field parameter.
- $Pr = \mu C_p / \kappa$ signifies the Prandtl number.
- $Ec = c^2 C_p / b$ is regarded as Eckert number.

The wall skin friction C_{fx}, C_{fy} and the local Nusselt number Nu_x are characterized by the following expressions:

$$C_{fx} = \frac{\tau_{zx}|_{z=0}}{\rho u_s^2}, \quad C_{fy} = \frac{\tau_{zy}|_{z=0}}{\rho u_w^2}, \quad Nu_x = \frac{x q_w}{k(T_w - T_\infty)}, \tag{3.14}$$

here τ_{zx} and τ_{zy} represent the stress tensors which can be evaluated directly from Eq. (3.1) as follows:

$$\tau_{zx} = \frac{\mu}{1 + \lambda_2}\{(u_z) + \lambda_1(uu_{xz} + vu_{yz} + wu_{zz})\}, \tag{3.15}$$

$$\tau_{zy} = \frac{\mu}{1 + \lambda_2}\{(v_z) + \lambda_1(uv_{xz} + vv_{yz} + wv_{zz})\}. \tag{3.16}$$

and $q_w = -\kappa(\partial T / \partial z)$ represents the surface heat flux. By using eq. (3.8), Eq. (3.14) will transformed in the following form:

$$Re_x^{\frac{1}{2}}C_{fx} = \frac{(1 + \beta)}{1 + \lambda_2}f''(0), \quad Re_x^{\frac{1}{2}}C_{fy} = \frac{(1 + \beta)}{1 + \lambda_2}g'(0), \quad Re_x^{-\frac{1}{2}}Nu_x = -\theta'(0), \tag{3.17}$$

in which $Re_x^{\frac{1}{2}}$ is representing the local Reynold number.

3.1.1. Newtonian fluid case:

The Newtonian fluid flow induced by the deforming surface is restored when $\lambda_2 = \beta = 0$. Eqs. (3.9)-(3.13) will presented as follow:

$$f''' + (ff'' - f'^2 + 2\lambda g) - Mf' = 0, \tag{3.18}$$

$$g'' + (fg' - f'g - 2\lambda f') - Mg = 0, \tag{3.19}$$

$$\theta'' + Pr(f\theta' - 2\theta f') + PrEc\{f''^2 + g'^2 + M(f'^2 + g^2)\}. \tag{3.20}$$

with the same conditions expressed in Eqs. (3.12)-(3.13).

3.2. Evaluation of entropy creation

The following equation gives entropy production rate per unit volume in Jeffrey fluid motion within a rotating frame of reference, considering the effects of viscous dissipation and Ohmic heating:

$$\dot{S}_{gen} = \frac{\kappa}{T_\infty^2}(T_z)^2 + \frac{\mu}{(1+\lambda_2)T_\infty}\left[(u_z)^2 + (v_z)^2 + \lambda_1\begin{Bmatrix} u(u_{xz}u_z + v_{xz}v_z) + vu_{yz}u_z \\ +vv_{yz}v_z + w(u_{zz}u_z + v_{zz}v_z) \end{Bmatrix}\right]$$
$$+ \frac{\mu}{T_\infty}(u^2 + v^2). \tag{3.21}$$

The right hand side of Eq. (3.21) consists of three parts: the initial term represents irreversibility caused by heat transfer that reflects entropy formation due to conduction; the second term depicts irreversibility due to fluid friction and the final term accounts for irreversibility effect arising from Ohmic heating.

The dimensionless entropy generation number, $N_G(\xi) = \dot{S}_{gen}T_\infty v/\kappa a(T_w - T_\infty)$, is introduced, and by applying Eq. (3.21) along with the similarity transformations (3.8), it assumes the following form:

$$N_G(\xi) = \alpha\theta'^2 + \frac{PrEc}{1+\lambda_2}\left\{f''^2 + g'^2 - \beta\left(\frac{f'f''^2 + f'g'^2}{-ff''f''' - fg'g''}\right)\right\} + MPrEc(f'^2 + g^2), \tag{3.21}$$

in which $\alpha = (T_w - T_\infty)/T_\infty$ signifies the temperature difference.

Bejan number:

An intriguing Bejan number Be is often computed to scrutinize entropy creation in boundary layer flows. It is defined as follows:

$$Be = \frac{\text{Entropy created by heat transfer}}{\text{overall entropy production}}. \tag{3.22}$$

In view of the above, the Bejan number Be in the current scenario is obtained as follows:

$$Be(\xi) = \frac{\alpha\theta'^2}{\alpha\theta'^2 + \frac{PrEc}{1+\lambda_2}\left\{f''^2 + g'^2 - \beta\left(\frac{f'f''^2 + f'g'^2}{-ff''f''' - fg'g''}\right)\right\} + MPrEc(f'^2 + g^2)}, \tag{3.23}$$

It is evident from Eq. (3.23) that the Bejan number (Be) ranges from 0 to 1. When Be approaches 0, heat transfer irreversibility is minimal. At $Be = 1/2$, both conduction and viscous (or Ohmic) heating contribute equally to the entropy generation. As Be approaches 1, irreversibility is predominantly driven by conduction.

3.3. Results and Discussion

Figs. 3.1(a)-3.1(d) depicts the graphical representations of total squared residual $E_{T,k}$ versus k for various values of λ_2, the ratio of relaxation to retardation time. With an increase in the order of OHAM approximations, these graphs shows a substantial decrease in $E_{T,k}$. Consequently, demonstrating the accuracy of HAM solutions.

Table 3.1 shows Comparsion of computational outcomes of skin friction coefficient and local Nusselt number using OHAM and the MATLAB scheme bvp5c for distinct values of controlling parameters. This data shows that the analytical results obtained by OHAM agrees very well with the numerical results obtained by bvp5c. Table 3.2 and Table 3.3 presents the numerical results by varying the values of different parameters. As the magnitude of λ_2, the ratio of relaxation to retardation time increases, the fluid has lower drag force that the least force needed to maintain linear deformation of surface drops. With increasing the values of Deborah number, the drag at surface will significantly enhances. Similarly, the stretching wall requires more force with an increase in rotational velocity. With an increase in λ_2, λ and Ec, the local nusselt number corresponding to surface cooling rate decreases. Conversely, Nu_x increases by raising the values of β.

Analytical results are worked out for the rotational motion of a Jeffrey fluid over a deforming plate, considering the effects of viscous dissipation. The physical explanation of the impact of various regulating parameters on the solution profiles is assigned in this section. In Figs. 3.2(a) through 3.2(d), graphical depictions of velocities u, v and w as well as temperature are presented across varying Deborah numbers. The Deborah number is associated with the retardation time, which is a measurement of how long it takes for a fluid to respond elastically to stress. The data suggests that extending the retardation time decreases momentum diffusion. This is evidenced by the velocity curves, which reach far-field conditions at greater distances from the plate as the β

values increase. Fig. 3.2(d) illustrates the impact of altering the Deborah number on the temperature profile. With an increment in β, the heat conduction effect diminishes because of increased convection apparent from the increased f in Fig. 3.2(c). For such reason, the temperature distribution appears to reduce as retardation time progresses.

Fig. 3.3(a)-3.3(d) illustrates how the relaxation to-retardation time ratio influences the velocity and temperature profile. When the relaxation time is longer, stress relaxation is slower and fluid tends to behave like elastic solid. The stream wise momentum diffusion is therefore shorter for a higher relaxation time. The reduction in momentum diffusion results in lower velocity distributions, as evidenced from the Figs. 3.3(a)-3.3(c). A decrease in the vertical velocity component suggests diminished convection, leading to a thicker thermal layer (refer to Fig. 3.3(d)).

Figs. 3.4(a)- 3.4(d) illustrate the rotational effects on the viscoelastic motion over the stretching plate. An increase in fluid's angular velocity is anticipated to offer more resistance to the stretching induced motion. Due to this, the horizontal and vertical velocities are reduced whenever rotation parameter λ is increased. Additionally, the rotating frame assumption causes the initiation of motion in the negative y-direction. As a result, this y-direction motion accelerates as the fluid's rotational speed increases. Because the vertical flow gets slower upon increasing rotation rate, the convection effect becomes less pronounced. This in turn boosts heat conduction resulting in a rise in thermal diffusion above the plate (see Fig. 3.4(d)).

Figs. 3.5(a)-3.5(d) include the plots of velocities and temperature across different magnetic interaction parameters. Lorentz force, which tends to resist the flow, induces a drag when a transverse magnetic field is set up in a direction normal to the flow. The viscous forces tend to rise as a result. Therefore, the decline in velocity in the boundary layer is observed in Fig. 3.5(a)-3.5(c). In Fig. 3.5(d) the intriguing phenomenon, known as Joule heating is introduced which is based on the concept that due to resistance heat is produced as the electric current flows through the conductor. An increment temperature profile results from an increase in M, which physically enhances the Joule heating effect, increasing the thermal layer thickness and permitting more heat generation.

Next, the impact of Prandtl number variation on the temperature curve is discussed via Fig. 3.6. Increasing Pr is expected to reduce the thickness of the thermal layer and increase the pace of

cooling since it quantifies the significance of momentum diffusion over thermal diffusion. This effect is shown in Fig. 3.6, where curves tend to grow steeper as Pr increases and move farther from the plate.

Fig. 3.7 demonstrates that the temperature profile progressively increases as the Eckert number Ec rises. A higher Eckert number can be interpreted as a more pronounced viscous dissipation term. Viscous dissipation which indicates the conversion of mechanical energy into thermal energy due to fluid's friction. In highly viscous fluids, the impact of viscous dissipation on the temperature profile should be more significant. Heat generation from frictional effects increases with increasing Eckert number. This results in an enhanced temperature profile.

Impact of varying β and λ_2 on local Nusselt number is demonstrated through Figs. 3.8(a) and 3.8(b). By raising the values of λ_2, the convection effects become more pronounced. This leads to increase in surface cooling rate. While opposite behavior is observed by varying the values of β.

Figs. 3.9(a) and 3.9(b) shows the profiles of entropy generation number for various values of temperature difference parameter α and Deborah number β. Figs. 3.10(a) and 3.10(b) shows the profiles of Bejan number for various values of temperature difference parameter α and Deborah number β.
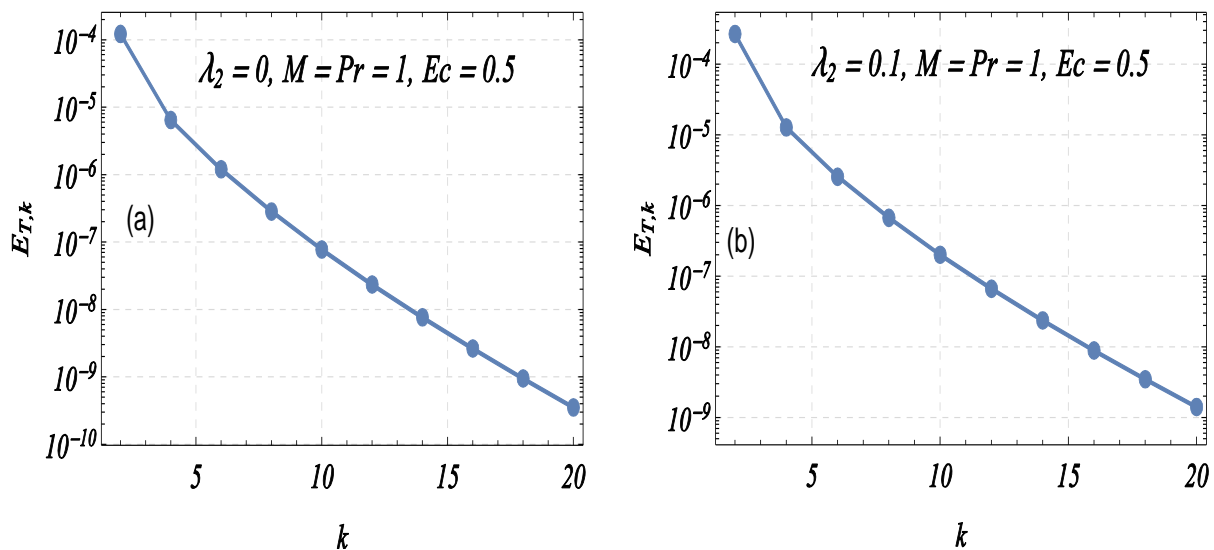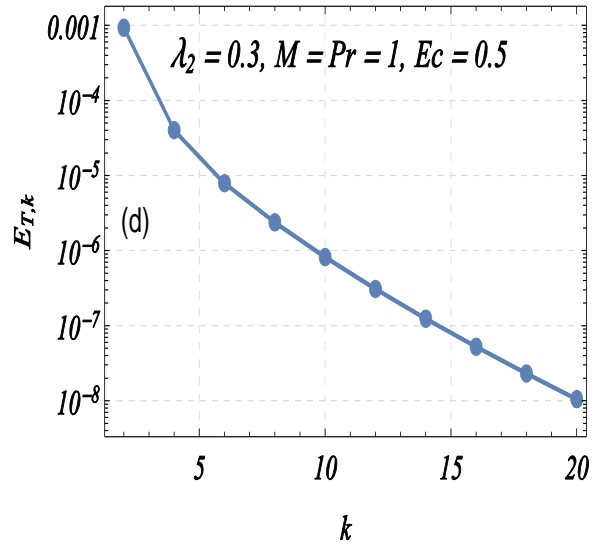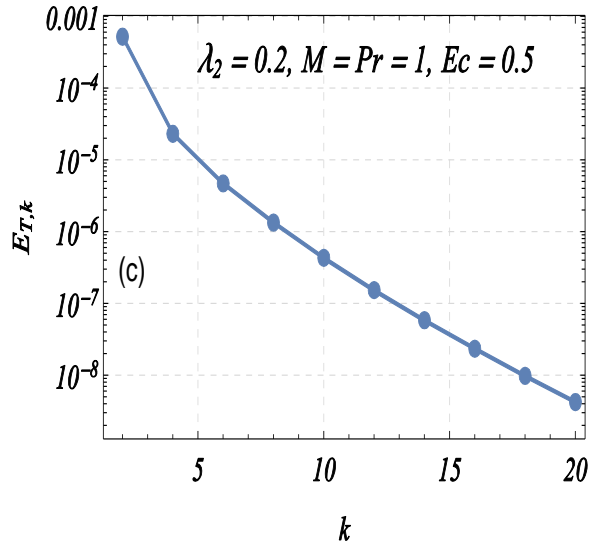
Figs. 3.1(a)-3.1(d): Graphical representation of overall averaged squared residual $E_{T,k}$ versus approximation Order k for various elasticity parameter K-values when $\lambda = \beta = 0.1$.

Table 3.1: Comparsion of computational outcomes of skin friction coefficient and local Nusselt number using OHAM and the MATLAB scheme bvp5c for distinct values of controlling parameters by keeping $Pr = 1, Ec = 0.5, M = 1$ and $\lambda_2 = 0.2$.

β	λ	$Re_x^{\frac{1}{2}}C_{fx}$		$Re_x^{\frac{1}{2}}C_{fy}$		$Re_x^{-\frac{1}{2}}Nu_x - \theta'(0)$	
		OHAM	Bvp5c	OHAM	Bvp5c	OHAM	Bvp5c
0.1	0.2	-1.36239	-1.36238	-0.14990	-0.14990	0.79475	0.79465
0.3		-1.48069	-1.48067	-0.16645	-0.16645	0.80646	0.80643
0.5		-1.59021	-1.58982	-0.18162	-0.18157	0.81398	0.81378
0.7		-1.69264	-1.69263	-0.19566	-0.19567	0.81872	0.81869
0.2	0.1	-1.41638	-1.41636	-0.07964	-0.07964	0.80976	0.80971
	0.2	-1.42277	-1.42275	-0.15837	-0.15837	0.80125	0.80119
	0.3	-1.43303	-1.43301	-0.23538	-0.23538	0.78755	0.78749
	0.4	-1.44666	-1.44663	-0.31010	-0.31010	0.76978	0.76924

Table 3.2: Analysis of skin friction variations with λ_2, the ratio of relaxation to retardation time, Deborah number β and rotation parameter λ for given conditions: $M = 1$, $Pr = 1$ and $Ec = 0.5$.

| λ_2	β	λ	$Re_x^{\frac{1}{2}}C_{fx} = \dfrac{(1+\beta)}{(1+\lambda_2)}f''(0)$	$Re_x^{\frac{1}{2}}C_{fy} = \dfrac{(1+\beta)}{(1+\lambda_2)}g'(0)$
0	0.3	0.2	-1.62202	-0.18234
0.2			-1.48069	-0.16645
0.4			-1.37085	-0.15410
0.6			-1.28231	-0.14415
0.2	0.1	0.2	-1.3624	-0.1499
	0.3		-1.48069	-0.16645
	0.5		-1.59021	-0.18162
	0.7		-1.69265	-0.19566
0.2	0.2	0.1	-1.41639	-0.07964
		0.2	-1.42278	-0.15837
		0.3	-1.43303	-0.23538
		0.4	-1.44666	-0.31010

Table 3.3: Analysis of local Nusselt number variations with λ_2, the ratio of relaxation to retardation time, Deborah number β, rotation parameter λ, and Eckert number Ec for given condition: $Pr = 1$ and $M = 1$.

| λ_2	β	λ	Ec	$-\theta'(0)$
0	0.3	0.2	0.5	0.81557
0.2				0.80661
0.4				0.79614
0.6				0.78488
0.2	0.1	0.2	0.5	0.79513
	0.3			0.80661
	0.5			0.81404
	0.7			0.81872
0.2	0.2	0.1	0.5	0.80995
		0.2		0.80149
		0.3		0.78789
		0.4		0.76978
0.2	0.2	0.1	0	1.21453
			0.5	0.80995
			1	0.40537
			1.5	0.00079
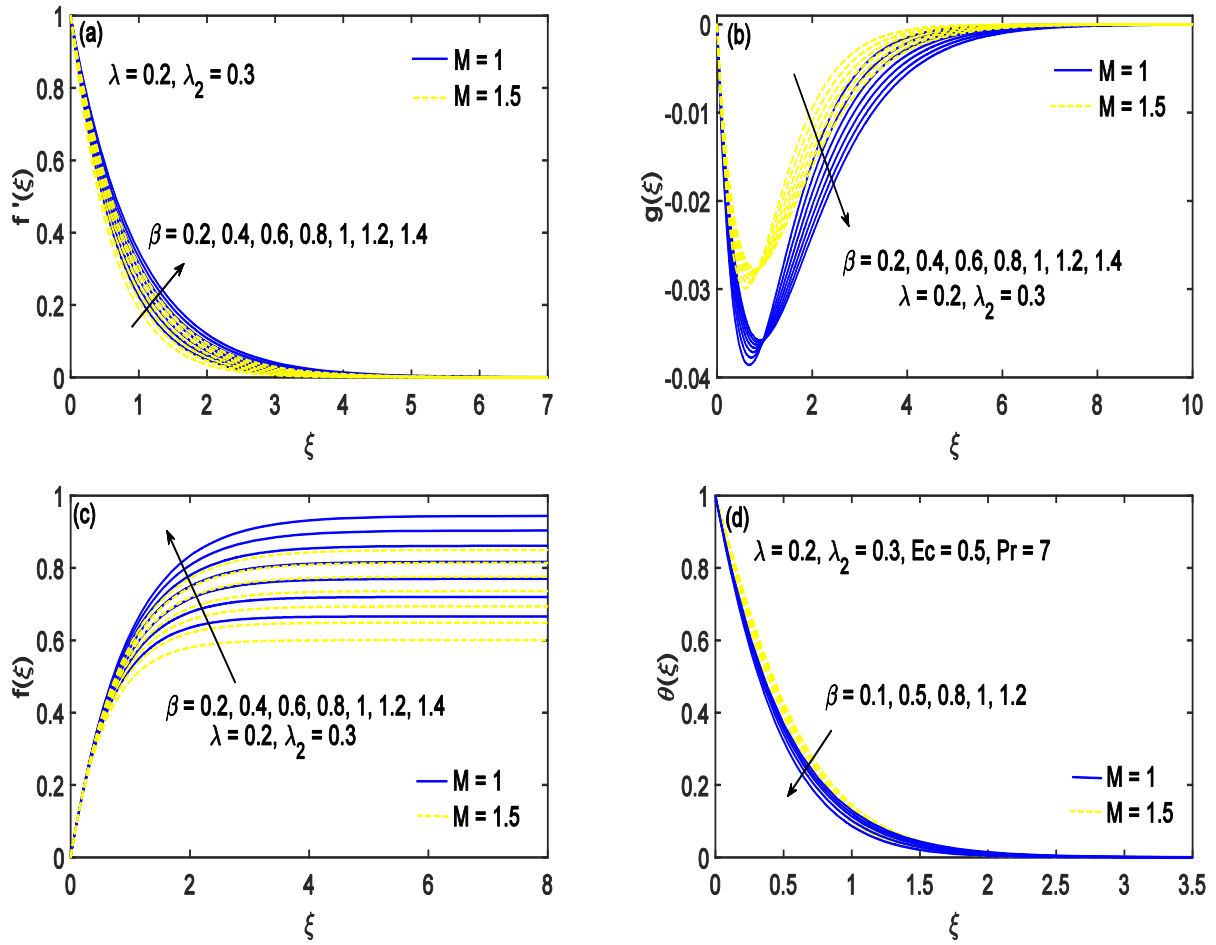
Figs. 3.2(a)-3.2(d): Impact of Deborah number β variation on the velocities (f', g and f) and temperature (θ) patterns.
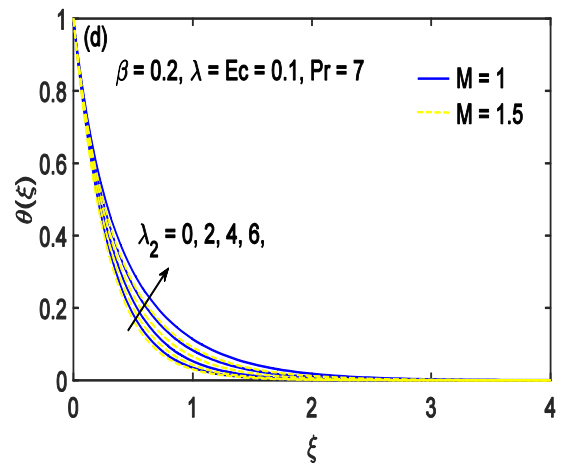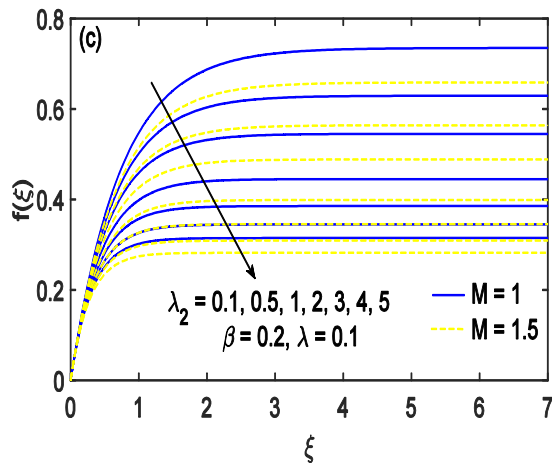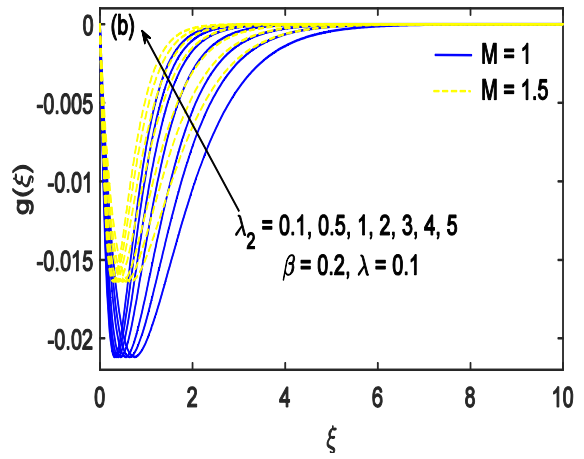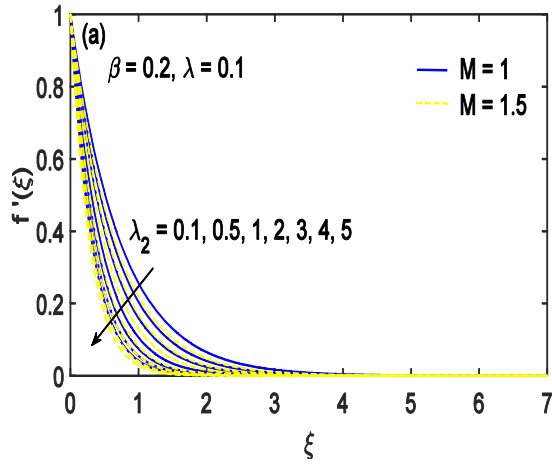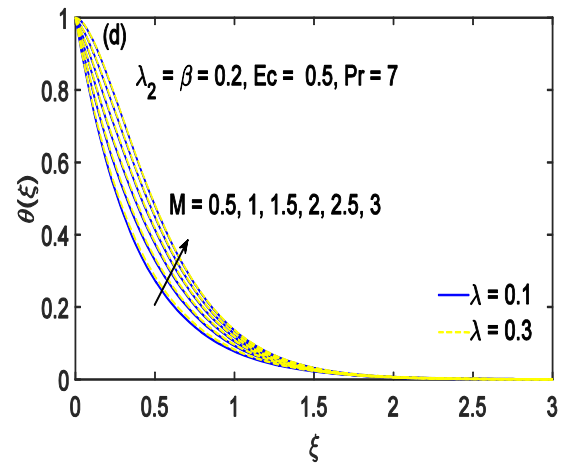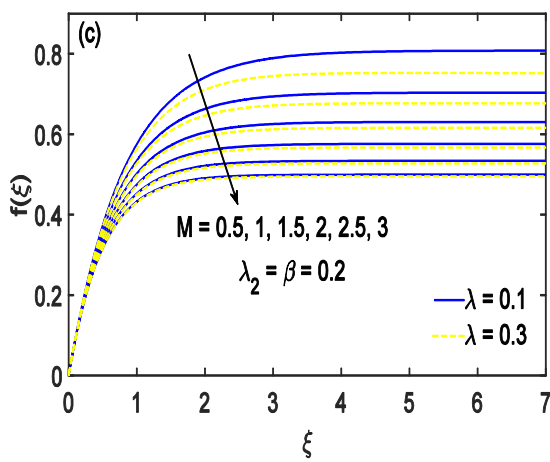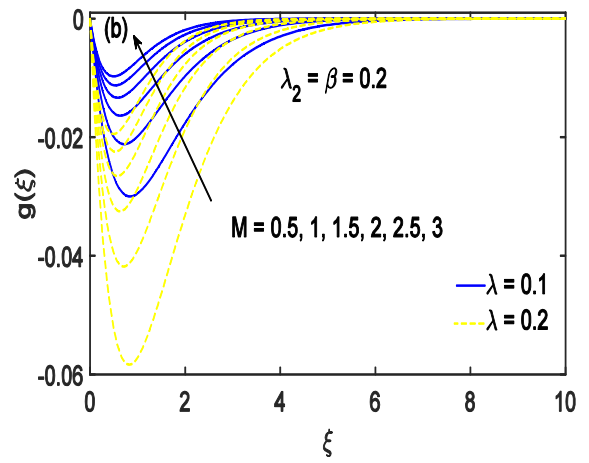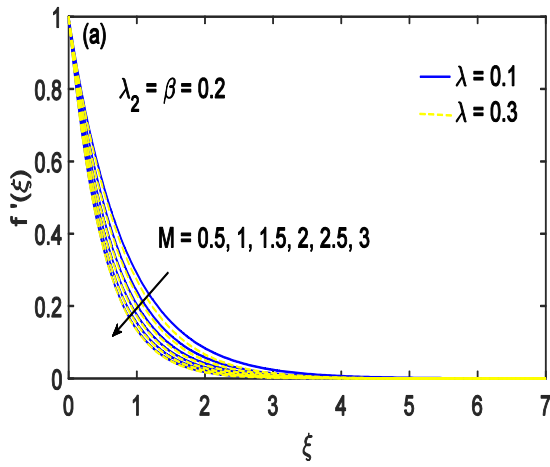
Figs. 3.3(a)-3.3(d): Impact of ratio of relaxation to retardation time λ_2 variation on the velocities (f', g and f) and temperature (θ) patterns.
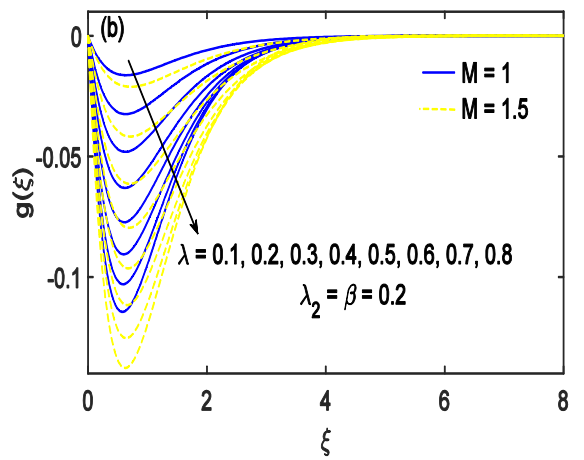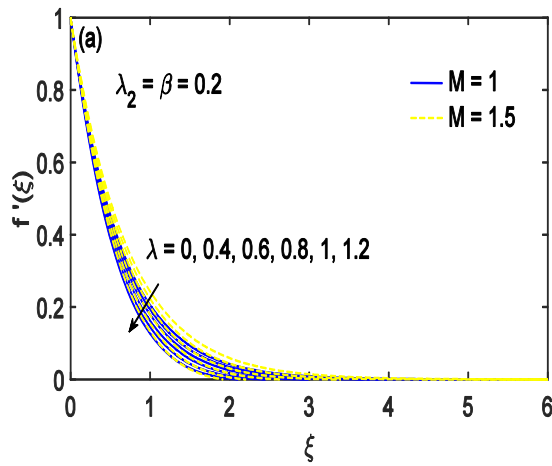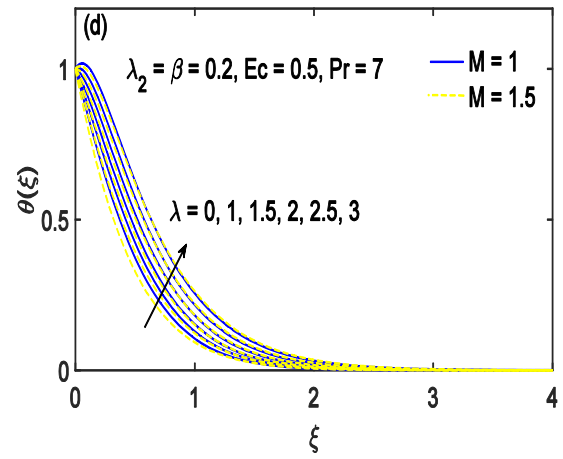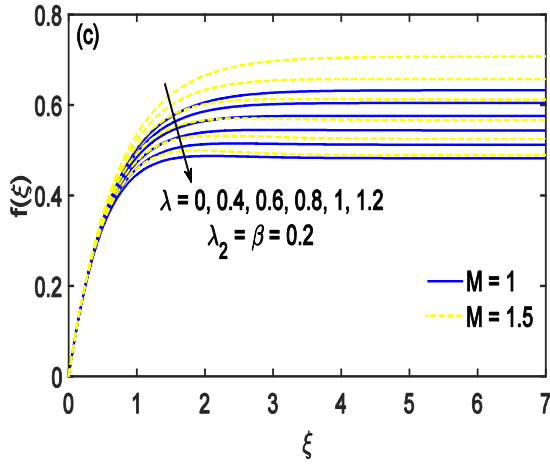
Figs. 3.4(a)-3.4(d): Impact of rotation parameter λ variation on the velocities (f', g and f) and temperature (θ) patterns.

Figs. 3.5(a)-3.5(d): Behavior of magnetic influence parameter M variation on the velocities (f', g and f) and temperature (θ) patterns.
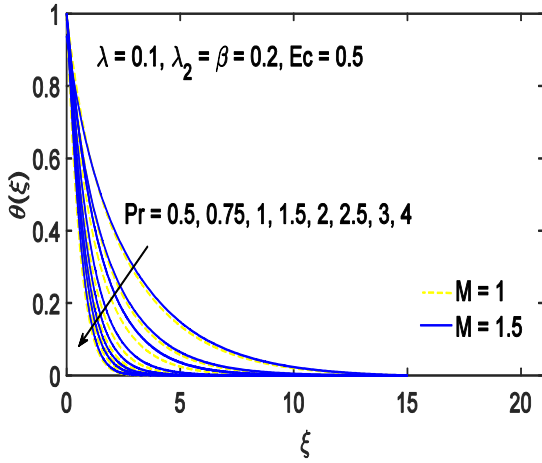

Fig. 3.6: Impact of Prandtl number Pr on the temperature (θ) dynamics.
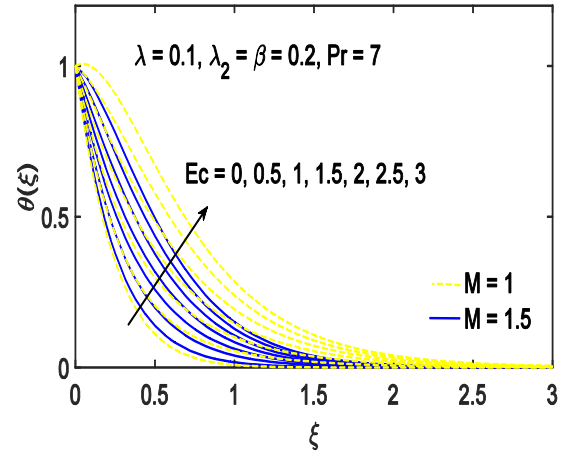
Fig. 3.7: Impact of Eckert number Ec on the temperature (θ) dynamics.
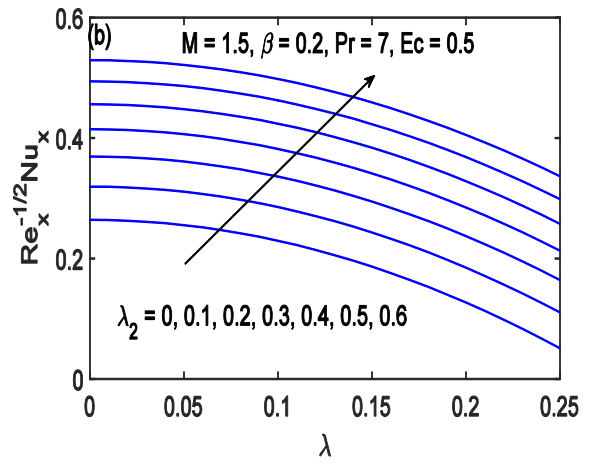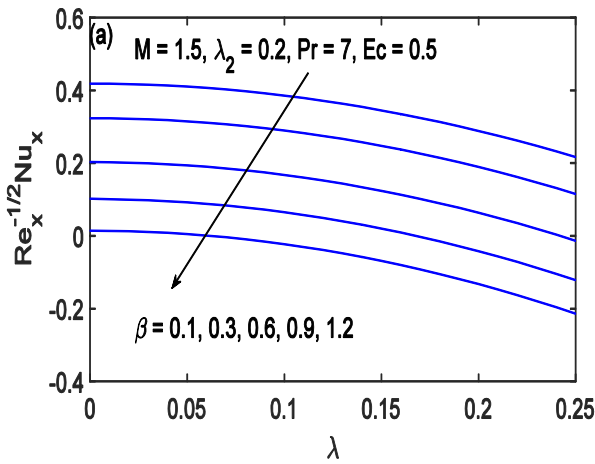
Figs. 3.8(a) and 3.8(b): Impact of Deborah number β and ratio of relaxation to retardation time λ_2 variation on the local Nusselt number.
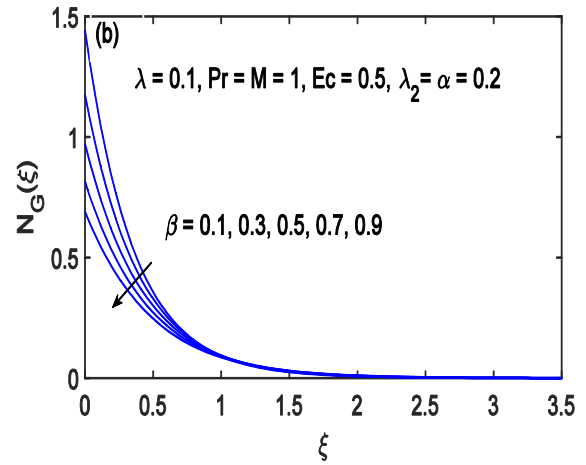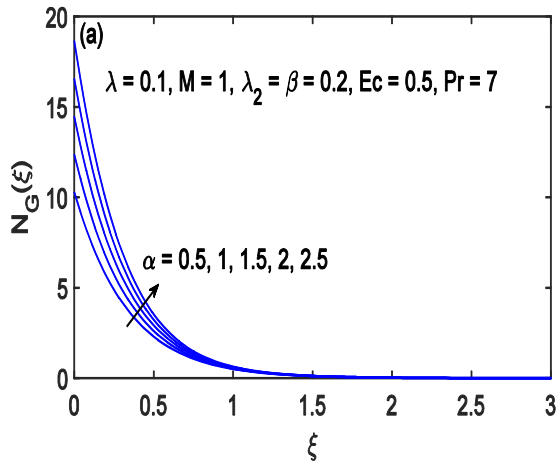
Figs. 3.9(a) and 3.9(b): Influence of temperature difference parameter α and Deborah number β on the entropy formation assessment.
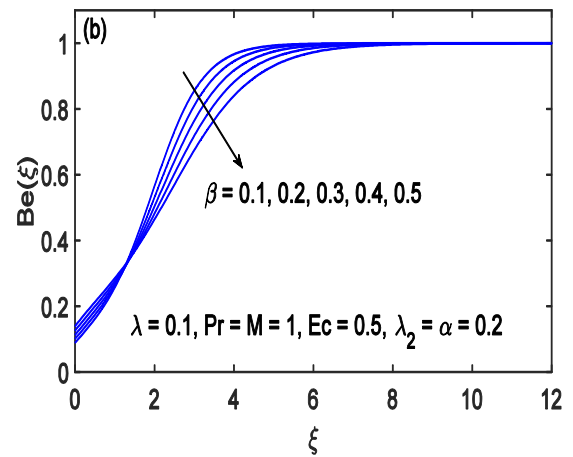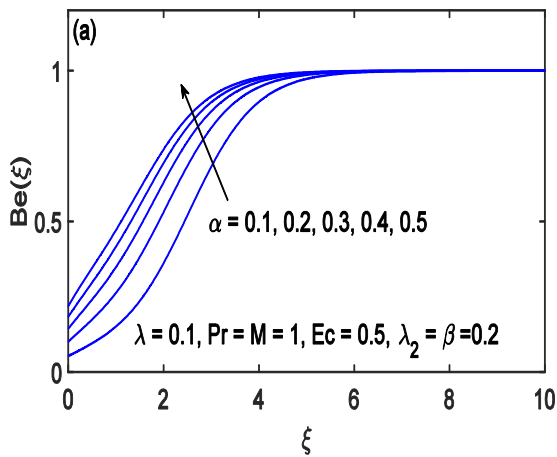
Figs. 3. 10 (a) and 3.10(b): Influence of temperature difference parameter α and Deborah number β on the Bejan number.

CHAPTER 4

Conclusion and future works

Analytical explorations of entropy production in Walters-B fluid and Jeffery fluid motions in a rotating frame are made through a well-known OHAM scheme. The obtained solutions are shown to be accurate through the computation of overall squared residuals of the governing system. The main observations of the study are summarized as follows:

o In Walters B fluid model, as the elasticity parameter K-values increase, a significant decline in the surface driving force is observed. On the other hand, the driving force variation with a higher λ is relatively minimal.

o The surface cooling rate declined because of raising elasticity parameter K. However, the fluid's rotational speed is found to assist the surface cooling rate.

o Increasing K leads to a significant reduction in momentum penetration, while simultaneously accelerating the y-direction flow generated by the rotating fluid.

o An appreciable augmentation in thermal penetration is witnessed as elasticity parameter rises.

o Interestingly, the inclusion of rotational effects leads to oscillations in the velocity profiles. Furthermore, a noticeable rise in local fluid temperature is observed as one raises parameter λ.

o By intensifying either viscous dissipation or the Joule heating effect, additional heat is produced within the boundary layer, resulting in increased thermal layer thickness.

o Enhancing the elasticity parameter K results in an increase in both entropy production rate and the Bejan number. A similar upward trend is observed when λ is increased.

o To attain convergent OHAM results, a 15th-order series solution is sufficient for both f and g, while a 25th-order approximation is required for θ, considering the specified range of parameters used in this study.

o The analytical method's precision becomes evident as the graph of the total squared residual decreases with increasing approximation order.

o The velocity profiles become increasingly thicker for growing increasing fluid's retardation time whereas opposite effect is witnessed as the ratio of relation to the retardation time grows.

o Enhancing the retardation time intensifies the vertical flow towards the plate, leading to a reduction in the $\theta-$profile and an increase in the cooling rate at the surface.

- The higher the temperature difference, greater the volumetric entropy generation rate. In contrast, the entropy production rate declines considerably as retardation time progresses.
- For sufficiently higher ratio of rotation rate to the stretch rate, the velocity curves are oscillatory decaying function of vertical distance.
- Consistent with earlier studies, incorporating the rotating frame results in motion along the negative y-axis. The effect of the fluid's rotation causes the momentum diffusion to decrease, while the temperature profile experiences a slight increase.

References

1. Jazaa, Y., Rehman, S., & Albouchi, F. (2024). On the enhancement of heat transport and entropy generation of the thin film flow of partially ionized non-Newtonian hybrid nanofluid. *Journal of the Taiwan Institute of Chemical Engineers*, *157*, 105412.

2. Nadeem, S., Ishtiaq, B., Alzabut, J., & Ghazwani, H. A. (2024). Entropy generation for exact irreversibility analysis in the MHD channel flow of Williamson fluid with combined convective-radiative boundary conditions. *Heliyon*, *10*(4).

3. Zhang, L., Zhang, H., Wang, S., Song, J., Yao, X., & Wang, W. (2024). Boundary layer and entropy analysis of non-Newtonian Casson nanofluids moving nonlinearly in a wedge-shaped stretching plate under an unsteady flow. *Case Studies in Thermal Engineering*, *56*, 104193.

4. Abdel-wahed, M. S., Ahmed, S. I., Mekheimer, K. S., & Sayed, A. Y. (2024). Entropy generation analysis of a micropolar fluid in a corrugated channel with convective and slip conditions. *Case Studies in Thermal Engineering*, *57*, 104283.

5. Ramesh, K., & Devakar, M. (2018). Influence of magnetohydrodynamics on peristaltic flow of a Walter's B fluid in an inclined asymmetric channel with heat transfer. *World Journal of Engineering*, *15*(4), 450-467.

6. Vaidya, H., Makinde, O. D., Choudhari, R., Prasad, K. V., Khan, S. U., & Vajravelu, K. (2020). Peristaltic flow of non-Newtonian fluid through an inclined complaint nonlinear tube: application to chyme transport in the gastrointestinal tract. *The European Physical Journal Plus*, *135*(11), 1-15.

7. Rani, J., Hina, S., & Mustafa, M. (2020). A novel formulation for MHD slip flow of elastico-viscous fluid induced by peristaltic waves with heat/mass transfer effects. *Arabian Journal for Science and Engineering*, *45*(11), 9213-9225.

8. Hafez, N. M., Alsemiry, R. D., Alharbi, S. A., & Abd-Alla, A. M. (2022). Peristaltic transport characteristics of a second-grade dusty fluid flown with heat transfer through a tube revisited. *Scientific Reports*, *12*(1), 21605.

9. Rafaqat, R., Khan, A. A., Zaman, A., Mabood, F., & Badruddin, I. A. (2022). Magnetohydrodynamics second grade compressible fluid flow in a wavy channel under peristalsis: Application to thermal energy. *Journal of Energy Storage*, *51*, 104463.

10. Ali, A., Awais, M., Al-Zubaidi, A., Saleem, S., & Marwat, D. K. (2022). Hartmann boundary layer in peristaltic flow for viscoelastic fluid: Existence. *Ain Shams Engineering Journal*, *13*(2), 101555.

11. Hayat, T., Ahmed, N., Sajid, M., & Asghar, S. (2007). On the MHD flow of a second grade fluid in a porous channel. *Computers & Mathematics with Applications*, *54*(3), 407-414.

12. Ali, W., Ali, F., ur Rahman, A., & Khan, I. (2023). A new model of time-dependent fractional second grade fluid for two-dimensional channel flow with heat transfer. *Alexandria Engineering Journal*, *81*, 7-16.

13. Seth, G. S., Mishra, M. K., & Tripathi, R. (2018). MHD free convective heat transfer in a Walter's liquid B fluid past a convectively heated stretching sheet with partial wall slip. *Journal of the Brazilian Society of Mechanical Sciences and Engineering*, *40*, 1-11.

14. Sarada, K., Gowda, R. J. P., Sarris, I. E., Kumar, R. N., & Prasannakumara, B. C. (2021). Effect of magnetohydrodynamics on heat transfer behaviour of a non-Newtonian fluid flow over a stretching sheet under local thermal non-equilibrium condition. *Fluids*, *6*(8), 264..

15. Cham, A., & Mustafa, M. (2023). Boundary layer formations over a stretchable heated cylinder in a viscoelastic fluid with partial slip and viscous dissipation effects. *Numerical Heat Transfer, Part A: Applications*, *85*(11), 1767–1779.

16. Gull, L., Mustafa, M., & Haq, R. U. (2024). A novel model for viscoelastic fluid flow and heat near a stretchable plate using variable fluid properties: A computational study. *Numerical Heat Transfer, Part B: Fundamentals*, *85*(6), 649-661.

17. Cham, A., Mustafa, M. (2024). Exploring the Dynamics of Second-Grade Fluid Motion and Heat Over a Deforming Cylinder or Plate Affected by Partial Slip Conditions. *Arab J Sci Eng* 49, 1505–1514.

18. Sadia, H., Mustafa, M., & Farooq, M. A. (2023). Numerical and series solutions for Von-Kármán flow of viscoelastic fluid inspired by viscous dissipation and Joule heating effects. *Alexandria Engineering Journal*, *75*, 181-190.

19. Das, A., & Sahoo, B. (2018). Flow and heat transfer of a second grade fluid between two stretchable rotating disks. *Bulletin of the Brazilian Mathematical Society, New Series*, *49*, 531-547.

20. Imtiaz, M., Kiran, A., Hayat, T., & Alsaedi, A. (2019). Joule heating and MHD effects in flow of second grade fluid due to a rotating disk with variable thickness. *Physica Scripta*, *94*(8), 085203.

21. Jafeer, M. B., & Mustafa, M. (2021). A study of elastico-viscous fluid flow by a revolving disk with heat dissipation effects using HAM based package BVPh 2.0. *Scientific Reports*, *11*(1), 4514.

22. C. Y. Wang, Stretching a surface in a rotating fluid, Z. angew. *Math. Phys*. 39 (1988) 177–185.

23. Rajeswari, V., & Nath, G. (1992). Unsteady flow over a stretching surface in a rotating fluid. *International Journal of Engineering Science*, *30*(6), 747-756.

24. Nazar, R., Amin, N., & Pop, I. (2004). Unsteady boundary layer flow due to a stretching surface in a rotating fluid. *Mechanics Research Communications*, *31*(1), 121-128.

25. Ahmed, J., Khan, M., & Ahmad, L. (2019). MHD swirling flow and heat transfer in Maxwell fluid driven by two coaxially rotating disks with variable thermal conductivity. *Chinese Journal of Physics*, *60*, 22-34.

26. Ahmed, A., Khan, M., Ahmed, J., & Hafeez, A. (2020). Von Kármán rotating flow of Maxwell nanofluids featuring the Cattaneo-Christov theory with a Buongiorno model. *Applied Mathematics and Mechanics*, *41*, 1195-1208.

27. Ali, B., Hussain, S., Nie, Y., Hussein, A. K., & Habib, D. (2021). Finite element investigation of Dufour and Soret impacts on MHD rotating flow of Oldroyd-B nanofluid over a stretching

sheet with double diffusion Cattaneo Christov heat flux model. *Powder Technology*, *377*, 439-452.

28. Ali, B., Thumma, T., Habib, D., & Riaz, S. (2022). Finite element analysis on transient MHD 3D rotating flow of Maxwell and tangent hyperbolic nanofluid past a bidirectional stretching sheet with Cattaneo Christov heat flux model. *Thermal Science and Engineering Progress*, *28*, 101089.

29. Akbar, S. S., & Mustafa, M. (2024). Coupled heat and mass transfer to viscoelastic fluid flow in a rotating frame using series and numerical solutions. *International Journal of Heat and Fluid Flow*, *106*, 109294.

30. T. Hayat, S. Asad, A. Alsaedi, F. E. Alsaadi, Radiative Flow of Jeffrey Fluid Through a Convectively Heated Stretching Cylinder, Journal of Mechanics, Volume 31, Issue 1, February 2015, Pages 69–78.

31. Megahed, A. M., & Reddy, M. G. (2021). Numerical treatment for MHD viscoelastic fluid flow with variable fluid properties and viscous dissipation. *Indian Journal of Physics*, *95*, 673-679.

32. Sadia, H., Mustafa, M. & Mehmood, T. (2024). Modeling slip flow of Bingham fluid induced by a porous revolving disk with viscous dissipation and Joule heating effects. *J Therm Anal Calorim* 149, 5555–5567.

33. Cham, A., & Mustafa, M. (2024). Boundary layer formations over a stretchable heated cylinder in a viscoelastic fluid with partial slip and viscous dissipation effects. *Numerical Heat Transfer, Part A: Applications*, *85*(11), 1767-1779.

34. Beard, D. W., & Walters, K. (1964, July). Elastico-viscous boundary-layer flows I. Two-dimensional flow near a stagnation point. In *Mathematical Proceedings of the Cambridge Philosophical Society* (Vol. 60, No. 3, pp. 667-674). Cambridge University Press.

35. Liao, S. J. (1992). The proposed homotopy analysis technique for the solution of nonlinear problems (Doctoral dissertation, Ph. D. Thesis, Shanghai Jiao Tong University).

36. Liao, S. (2010). An optimal homotopy-analysis approach for strongly nonlinear differential equations. *Communications in Nonlinear Science and Numerical Simulation*, *15*(8), 2003-2016.

37. Shehzad, S. A., Hayat, T., Alsaedi, A., & Obid, M. A. (2014). Nonlinear thermal radiation in three-dimensional flow of Jeffrey nanofluid: a model for solar energy. *Applied Mathematics and Computation*, *248*, 273-286.